

Pulsating chromosphere of classical Cepheids

Calcium infrared triplet and $H\alpha$ profile variations^{*}.

V. Hocdé¹, N. Nardetto¹, S. Borgniet², E. Lagadec¹, P. Kervella², A. Mérand³, N. Evans⁴, D. Gillet⁵, Ph. Mathias⁶,
A. Chiavassa¹, A. Gallenne¹, L. Breuval², and B. Javanmardi²

¹ Université Côte d’Azur, Observatoire de la Côte d’Azur, CNRS, Laboratoire Lagrange, France,
email : vincent.hocde@oca.eu

² LESIA (UMR 8109), Observatoire de Paris, PSL, CNRS, UPMC, Univ. Paris-Diderot, 5 place Jules Janssen, 92195 Meudon,
France

³ European Southern Observatory, Karl-Schwarzschild-Str. 2, 85748 Garching, Germany

⁴ Smithsonian Astrophysical Observatory, MS 4, 60 Garden St. Cambridge MA 02138

⁵ Observatoire de Haute-Provence – CNRS/PYTHEAS/Université d’Aix-Marseille, 04870 Saint-Michel l’Observatoire, France

⁶ IRAP, Université de Toulouse, CNRS, CNES, UPS. 14 Av. E. Belin, 31400 Toulouse, France

Received ... ; accepted ...

ABSTRACT

Context. It has been shown recently that the infrared emission of Cepheids, which is constant over the pulsation cycle, might be due to a pulsating shell of ionized gas of about 15% of the stellar radius, which could be attributed to the chromospheric activity of Cepheids.
Aims. The aim of this paper is to investigate the dynamical structure of the chromosphere of Cepheids along the pulsation cycle and quantify its size.

Methods. We present $H\alpha$ and Calcium Near InfraRed triplet (Ca IR) profile variations using high-resolution spectroscopy with the UVES** spectrograph of a sample of 24 Cepheids with a good period coverage from ≈ 3 to 60 days. After a qualitative analysis of the spectral lines profiles, we quantify the Van Hoof effect (velocity gradient between the $H\alpha$ and Ca IR) as a function of the period of the Cepheids. Then, we use the Schwarzschild mechanism (a line doubling due to a shock wave) to quantify the size of the chromosphere.

Results. We find a significant Van Hoof effect for Cepheids with period larger than $P = 10$ days, in particular $H\alpha$ lines are delayed with a velocity gradient up to $\Delta v \approx 30$ km/s compared to Ca IR. By studying the shocks, we find that the size of the chromosphere of long-period Cepheids is of at least $\approx 50\%$ of the stellar radius, which is consistent at first order with the size of the shell made of ionized gas previously found from the analysis of infrared excess. Last, for most of the long-period Cepheids in the sample, we report a motionless absorption feature in the $H\alpha$ line that we attribute to a circumstellar envelope that surrounds the chromosphere.

Conclusions. Analyzing the Ca IR lines of Cepheids is of importance to potentially unbiased the period-luminosity relation from their infrared excess, particularly in the context of forthcoming observations of radial velocity measurements from the Radial Velocity Spectrometer (RVS) on board *Gaia*, that could be sensitive to their chromosphere.

Key words. Techniques : Spectrometry – stars: variables: Cepheids – stars: chromospheres – shock waves

1. Introduction

Cepheids are milestones of the extragalactic distance scale since their period and luminosity are correlated, which is known as the Leavitt law (Leavitt 1908) also called the period-luminosity relation (hereafter PL relation). These variable stars have provided among the most essential advances in the history of astronomy from the discovery of galaxies to the expansion of the Universe (Hubble 1926, 1929). Still today, the discovery of the accelerated expansion of the Universe (Riess et al. 1998) has demonstrated the central importance of Cepheids in modern astronomy. However, uncertainties on both zero point and slope of the PL relation are today one of the largest contributors to the error on the extragalactic distance ladder and therefore on the determination of H_0 , the Hubble-Lemaître constant (Riess et al. 2019).

^{*} Based on observations made with ESO telescopes at Paranal observatory under program IDs: 098.D-0379(A), 0100.D-0397(A) and 0101.D-0551(A)

^{**} Ultra Violet and Echelle Spectrograph project developed by the European Southern Observatory.

A plausible source of uncertainty could be due to InfraRed (IR) excess emitted by CircumStellar Envelope (CSE) such as the ones discovered using long-baseline interferometry (Kervella et al. 2006; Mérand et al. 2006) in the K-band. However the origin and the nature of these CSEs are still debated. In particular, while CSE emission is explained by dust emission in some cases (Gallenne et al. 2012, 2013; Groenewegen 2020), it fails to reproduce the IR excess in other studies (Schmidt 2015).

The extended and dynamical atmosphere of Cepheids could be at the origin for the observed IR excess. Recently, Hocdé et al. (2020) analytically modeled free-free and bound-free emission from a thin shell of ionized gas to explain the near and mid-IR excess of Cepheids. This shell is modeled with a size of about 15% of the star radius, whatever the pulsation phase, which corresponds to the region of the lower chromosphere. In this model the ionized material could be provided by periodic shocks occurring in the atmosphere, which heat up and ionize the gas.

Shocks in radially pulsating atmosphere of Cepheids have been largely studied in the $H\alpha$ Balmer line, providing valuable insight to the atmosphere dynamics (Breitfellner & Gillet

1993a,b,c; Nardetto et al. 2008; Gillet 2014). These studies have also been supported by radiative hydrodynamic models (Fokin 1991; Fokin et al. 1996; Fadeyev & Gillet 2004) which have demonstrated how the shock waves are generated then propagated through the atmosphere during a pulsation cycle. These studies emphasized the fundamental differences on the dynamics depending on short, medium or long pulsation period of Cepheids. In addition, the $H\alpha$ emissions reported in the latter studies, in particular in upper atmosphere of long-period Cepheids, could indicate a chromospheric emission of pulsational origin.

Chromospheric activity of Cepheids has been first probed using optical Ca II K line (Wilson & Vainu Bappu 1957; Kraft 1957) which showed transitory emissions after minimum light, with an increasing duration and strength with pulsation period. Later, upper chromospheric emission was detected on β Dor using ultraviolet Mg II h and k (Schmidt & Weiler 1979) followed by Schmidt & Parsons (1982, 1984) who found heterogeneous emissions in the chromosphere with both rising and falling materials traveling through tenth of stellar radii.

Then, in the most outer part of the chromosphere, Sasselov & Lester (1994c) observed a steady outflow of infrared He I $\lambda 10830$ absorption line, while time-dependent and non-LTE hydrodynamic modeling constrained by previously published observational data (Sasselov & Lester 1994b,a) show that the upper chromosphere should be permanently heated by an acoustic or magneto-hydrodynamic energy provided by mean of convection. Hence, a combination of both low-frequency excitation provided by pulsational shocks and persistent high-frequency acoustic heating from turbulent convection cells seem to be responsible for the chromospheric dynamics. Others mechanisms leading to high temperature plasmas (10^6 K) are not excluded. Indeed Bohm-Vitense & Parsons (1983) possibly detected X-ray emission in the spectra of ζ Gem, probably due to a chromospheric activity, which has been confirmed later, around $\phi = 0.5$ in the case of δ Cep and β Dor (Engle et al. 2017). Although several heating mechanisms to produce such amount of energy are considered, for example fast-moving shocks or magnetic reconnections, a coherent physical explanation is still to be provided.

Alternative lines for probing upper atmosphere dynamic and chromospheric activity are provided by the calcium infrared triplet ($\lambda 8498.018$, 8542.089 and 8662.140\AA). Indeed, Linsky et al. (1970) have shown first that Ca IR lines from the Sun are formed in the lower chromosphere. These lines are also sensitive to the temperature since they are collisionally controlled like Ca H and K lines, between which an empirical correlation has been determined (Martin et al. 2017). These properties make Ca IR a suitable indicator of chromospheric activity (Linsky et al. 1979; Foing et al. 1989; Chmielewski 2000; Busà et al. 2007). While the emission in the core is generally weaker than other chromospheric indicators these lines have the advantage not to be blended by circumstellar or interstellar absorption contrary to Ca H and K and Mg II h and k . A series of paper on the solar chromosphere has also highlighted the importance of studying Ca IR complementary to $H\alpha$ for probing the chromospheric activity (Cauzzi et al. 2008; Vecchio et al. 2009; Reardon et al. 2009; Cauzzi et al. 2009). Indeed, as shown by Vernazza et al. (1973), the formation region of $H\alpha$ and Ca IR covers most of the low chromosphere in the Sun. Therefore, it is interesting to use modern high-resolution instrument capabilities to observe Ca IR complementary to $H\alpha$ line for studying the pulsating chromosphere of classical Cepheids.

In addition, Ca IR lines were recently used to measure radial velocities (RVs) in Cepheids' atmospheres (Wallerstein et al.

2015, 2019). Indeed, as stated by Wallerstein et al. (2019), since the Radial Velocity Spectrometer (RVS) of ESA *Gaia* survey observes in the same wavelength range (Munari 1999; Sartoretti et al. 2018; Katz et al. 2019), it is of prime importance to understand the dynamic of these lines for Cepheid RV measurement accuracy, in particular in the context of the use of the Baade-Wesselink method for extragalactic distance scale measurement. The paper is structured as follows. We first present the UVES high-resolution profiles of $H\alpha$ and Ca IR for the 24 Cepheids in our sample in Sect. 2. We analyze $H\alpha$ and Ca IR profiles variations in Sect. 3 and Sect. 4, respectively. In Sect. 5, we study the dynamics of the chromosphere from the Van Hoof effect. We finally estimate the size of the chromosphere from the Schwarzschild mechanism observed in Ca IR in Sect. 6. We then discuss our results in Sect. 7 and conclude in 8.

2. UVES observations and Data reduction

2.1. Observations and data reduction

We gathered 1350 high-resolution ($R \sim 75000$) spectra from 24 Cepheids acquired with the red arm (~ 570 to ~ 940 nm wavelength range) of the UVES spectrograph (Dekker et al. 2000) mounted on the UT2 telescope at the Very Large Telescope (VLT). The processing and normalization of these spectra are detailed in Borgniet et al. (2019). We acquired several consecutive spectra (up to a dozen) at each observing epoch. The total number of distinct observing epochs is 193 over the whole data sample, with an average number of 8 epochs per target. The total number of epoch per target is indicated in Table 1. The average SNR per single spectrum is ≈ 100 . In order to discuss qualitatively the spectral line profiles, at a given epoch, we consider only the first snapshot of a series, without averaging the consecutive spectra. We consider the different observing epochs to be part of a unique pulsation cycle for each target, despite possible cycle-to-cycle variations (Anderson 2016). To study the line profile variations, we focus on the core of each line, hence we consider the same RV window ranging from -200 to 200 km/s and centered on the line rest wavelength corrected by the star center-of-mass velocity (also called γ -velocity, V_γ). The V_γ values we consider in the following of the analysis are listed in Table 1. We present an UVES spectrum centered on the Ca IR triplet in Fig. 1. AX Cir (5.27d), S Nor (9.75d) and VZ Pup (23.17d) are considered as prototypes of small-, mid-, and long-periods respectively in the following of the paper, because of their good phase coverage (see Figs. 2, 3 and 4) and recent ephemeris (see Table 1) presented in next section.

2.2. Ephemeris

It is essential to use accurate ephemeris to analyze the profile variations of Cepheids along their pulsation cycle with precision. Ephemeris of Cepheids are characterized by their pulsation period P and their referenced epoch T_0 given at maximum light. However, since Cepheids undergo period change with time depending on evolutionary state (Turner et al. 2006), it is necessary to use ephemeris with reference epoch which is close to UVES date of observation. Modified Julian Date (MJD) of the UVES observations is approximately 58000, which renders suitable ephemeris obtained from *Gaia* Collaboration (2018). When these ephemeris are unavailable we use SpectroPhoto-Interferometric modeling of Pulsating Stars (SPIPS) which is a model-based parallax-of-pulsation code. SPIPS gathers multiple different data sets available in the literature from photo-

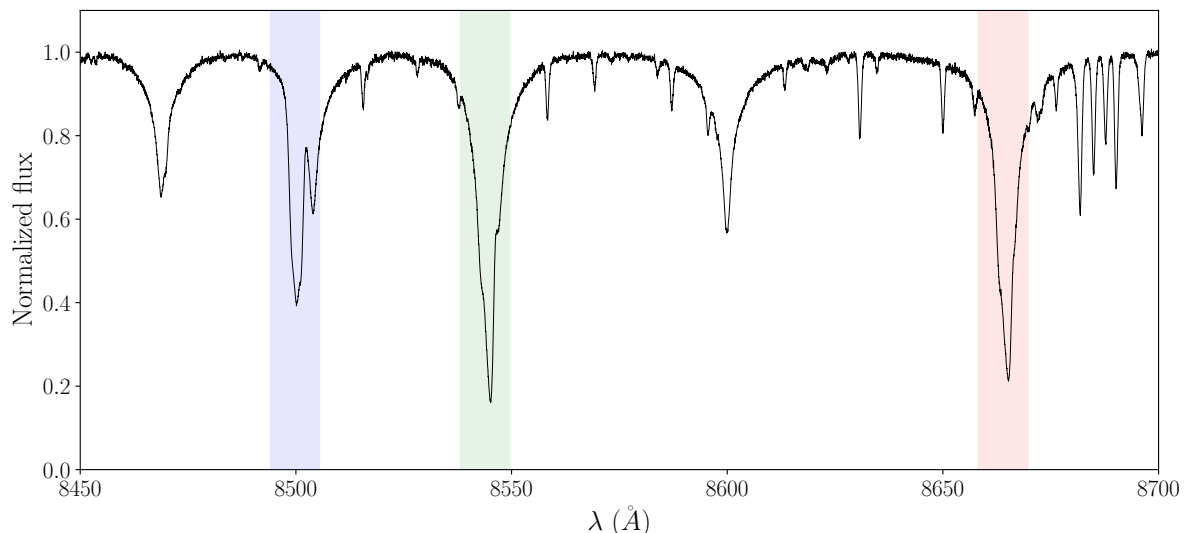


Fig. 1: Typical normalized UVES spectrum plotted over the RVS spectral window. Calcium infrared triplet at 8498, 8552 and 8662 angstroms for VZ Pup at $\phi = 0.91$ is presented. In the following the spectral line profiles are plotted over the $[-200,+200]$ km/s velocity range, represented by vertical strips around each line.

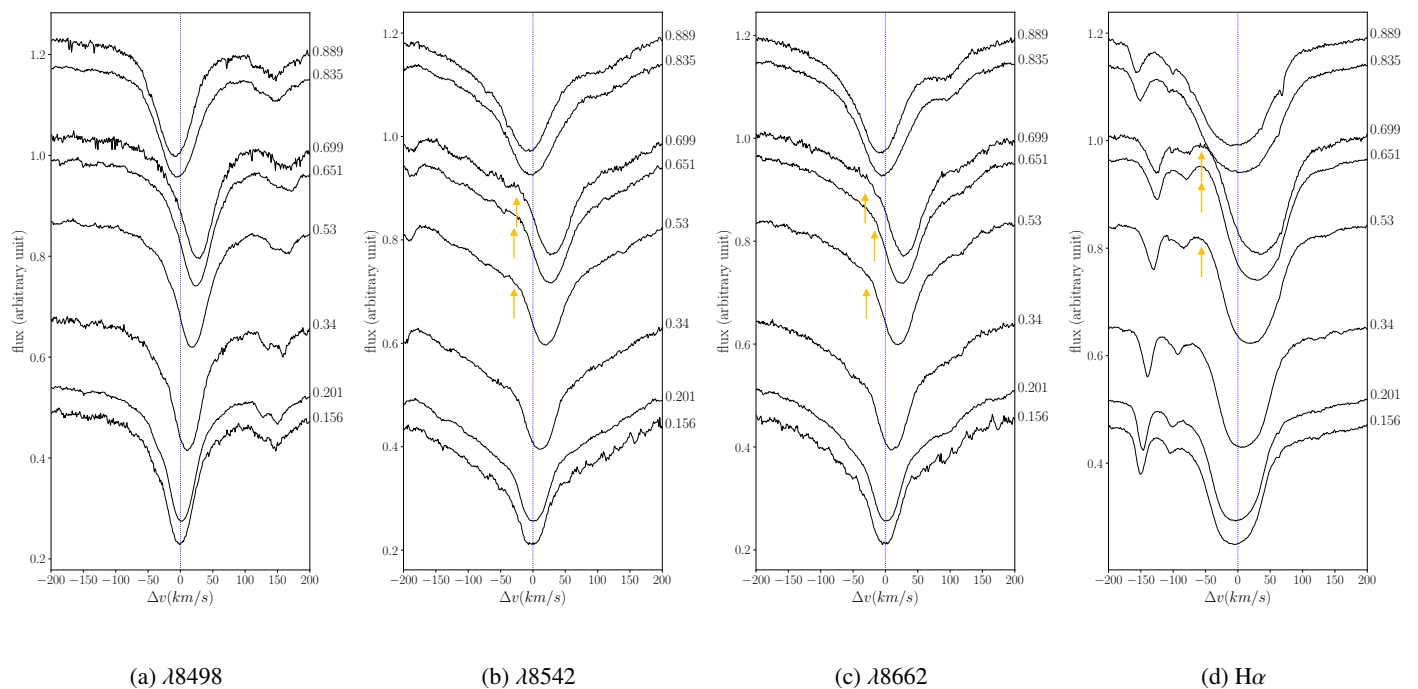


Fig. 2: AX Cir, 5.27d. Colored arrows refer to remarkable features in these profiles and are also associated to the color from Fig. 6. Orange arrow is the blue-shifted emission due to a blended inverse P Cygni profile.

metric, interferometric, effective temperature and radial velocity measurements in a robust model fit (Mérand et al. 2015). SPIPS was already extensively introduced and used in several studies (Mérand et al. 2015; Breifelder et al. 2016; Kervella et al. 2017; Galleme et al. 2017; Hocdé et al. 2020). When stars are not found in the precedent methods, which is the case for four stars, we retrieve data from the General Catalogue of Variable Stars

¹ (GCVS, Samus' et al. 2017) or the American Association of Variable Star Observers ² (AAVSO, Watson et al. 2006). We note that older ephemeris could introduce a phase shift in the radial velocity curves, in particular in the case of the long period V 1496

¹ <http://www.sai.msu.su/gcvs/gcvs/>

² <http://vizier.u-strasbg.fr/viz-bin/VizieR?-source=B/vsx>

Table 1: The γ -velocities of the stars in the sample are indicated together with the corresponding references. The ephemeris (T_0 , P) are retrieved either from [Gaia Collaboration \(2018\)](#) (G18), SPIPS software or the GCVS catalogue. Otherwise, the ephemeris of EW Sct and V1496 Aql are retrieved from AAVSO and [Berdnikov et al. \(2004\)](#), respectively. The number of UVES epoch of observations is indicated in the last column. The Cepheids that we consider as prototypes in the following of the paper are indicated in bold.

Star	γ (km/s)	Ref.	P (days)	T_0 (MJD)	Ephemeris	UVES epoch
AV Cir	8.7 \pm 1.6	(1)	3.065255	56890.9571	G18	10
BG Cru	-19.3 \pm 2.2	(2)	3.342477	56965.8567	G18	6
RT Aur	20.3 \pm 0.3	(2)	3.728313	47956.8877	SPIPS	7
AH Vel	26.0 \pm 2.9	(2)	4.226461	56915.1433	G18	7
AX Cir	-20.9 \pm 4.6	(2)	5.275967	56887.7452	G18	8
MY Pup	11.0 \pm 2.9	(2)	5.692962	56948.3850	G18	7
EW Sct	-18.6 \pm 0.3	(2)	5.82363	49705.23	AAVSO	9
U Sgr	2.8 \pm 0.3	(2)	6.745332	48336.5001	SPIPS	10
V636 Sco	9.1 \pm 0.17	(3)	6.79671	40364.392	GCVS	7
R Mus	3.8 \pm 2.9	(2)	7.510276	56912.6852	G18	6
S Mus	-1.9 \pm 0.4	(3)	9.658900	56867.6654	G18	7
β Dor	7.2 \pm 0.7	(2)	9.842661	50274.9261	SPIPS	5
S Nor	5.6 \pm 0.05	(4)	9.753759	56874.8021	SPIPS	7
ζ Gem	2.8 \pm 0.2	(2)	10.149857	48708.0588	SPIPS	6
TT Aql	3.0 \pm 0.3	(2)	13.754750	48308.5570	SPIPS	10
RU Sct	-4.8 \pm 0.3	(2)	19.70445	48335.5908	SPIPS	7
RZ Vel	24.1 \pm 2.4	(2)	20.497635	56875.8093	G18	5
WZ Car	-14.7 \pm 2.7	(2)	23.01759	53418.78	GCVS	10
VZ Pup	63.3 \pm 2.7	(2)	23.172844	56904.7167	G18	8
T Mon	30.4 \pm 0.2	(2)	27.029570	43783.7905	SPIPS	6
ℓ Car	3.3 \pm 0.7	(2)	35.55783	50583.7427	SPIPS	6
U Car	1.7 \pm 2.3	(2)	38.717914	56849.1763	G18	8
RS Pup	24.6 \pm 0.5	(2)	41.464114	56872.3158	G18	5
V1496 Aql	71.8 \pm 5.8	(1)	65.3679	51736.0660	(5)	8

- (1): [Gaia Collaboration \(2018\)](#),
(2): [Gontcharov \(2006\)](#),
(3): [Pourbaix et al. \(2004\)](#),
(4): [Mermilliod et al. \(2008\)](#),
(5): [Berdnikov et al. \(2004\)](#)

Aql which is known to present a significant stochastic period change ([Berdnikov et al. 2004](#)). The ephemeris are presented in Table 1 while profile variations are shown in Appendix B.

In the next sections, we proceed in two steps to analyze the data: we first describe the $H\alpha$ profiles as an observational basis, then, we analyze Ca IR profiles.

3. Observational basis: $H\alpha$ profile variations

In this section, we mostly confirm the $H\alpha$ line behaviour which has been found in previous studies, but for a larger sample of 24 Cepheids with a good period coverage from $P \approx 3$ to 60 days.

3.1. Short-period cepheids $P < 10d$

Several studies have reported the quiescent behaviour of $H\alpha$ profiles of short-period cepheids which indeed present similar behaviour than other metallic absorption lines ([Schmidt 1970](#); [Nardetto et al. 2008](#)), while some authors have found differences at some phases ([Jacobsen & Wallerstein 1981](#)). The UVES observations of the 10 short-period Cepheids in the sample confirm this general trend, with quiescent profiles during most of the pulsation cycle. At some phases, half of the short-period Cepheids present more disturbed features, especially a weak blue-shifted

emission is observed between phase $\phi = 0.6-0.9$ (see orange arrow in Fig. 2d). Because of the gravitational acceleration, upper atmosphere descending layers can reach supersonic velocities, producing an inward radiative shock. An inverse P Cygni profile could appear when the column density is important enough to contribute to the emission. However, the classical 0 km/s emission in P Cygni profile is blended with deep photospheric absorption, resulting in an apparent blue-shifted emission (see Fig. 5a). This emission in short-periods is followed by an important enlargement of the line profile, which is usually attributed to an increase of the turbulence during atmosphere compression ([Breitfellner & Gillet 1993a](#); [Fokin et al. 1996](#)).

3.2. Medium-period cepheids $P \approx 10d$

Medium-period Cepheids differ from the short- and long-period Cepheids by the shape of their radial velocity curve due to the Hertzsprung progression ([Hertzsprung 1926](#)). These Cepheids are indeed close to the $\omega_2/\omega_0 = 0.5$ resonance, where ω_0 and ω_2 are the periods corresponding to the fundamental and the second overtone modes respectively ([Kovacs et al. 1990](#)). The UVES sample of medium-period Cepheids contains four stars, namely S Nor (our prototype), S Mus, ζ Gem and β Dor, with a rather poor pulsation coverage. These stars have been studied by several authors ([Bell & Rodgers 1967](#); [Schmidt 1970](#); [Jacobsen &](#)

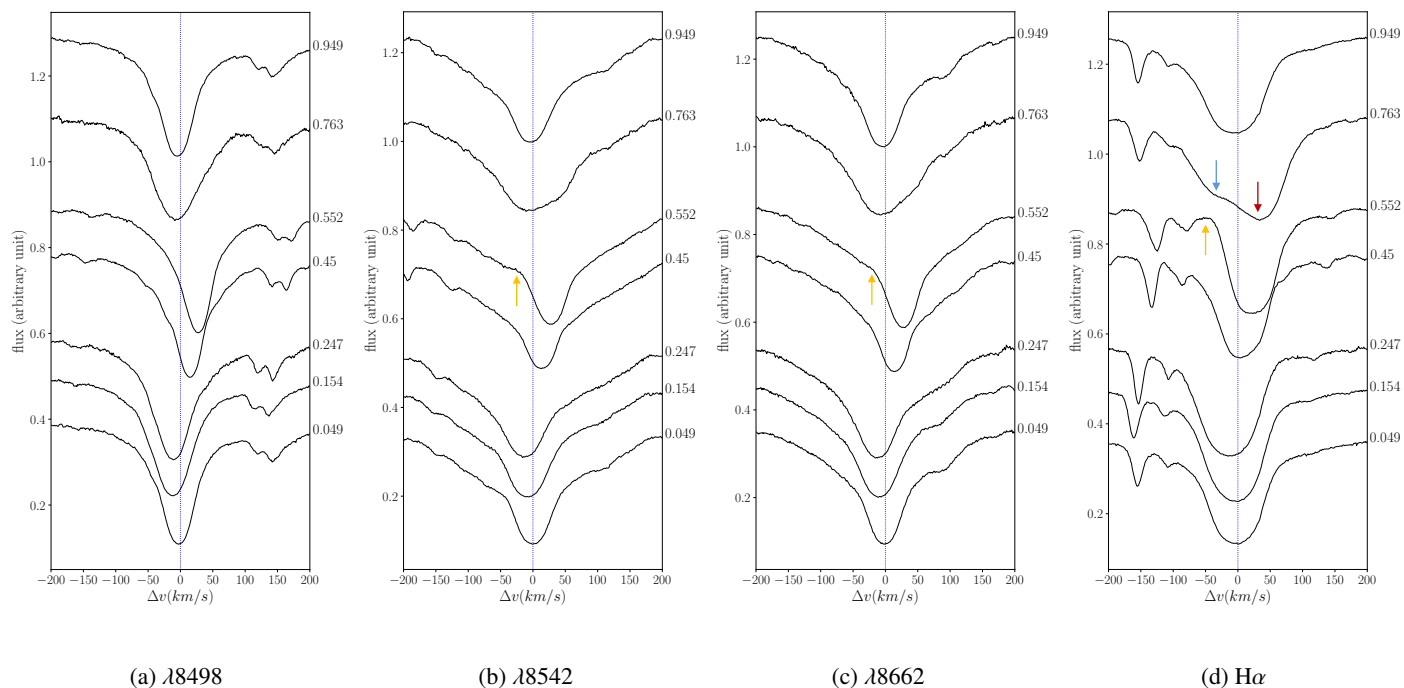


Fig. 3: S Nor, 9.75d. Blue arrow is the blue-shifted absorption due to the main shock. Red arrow is the red-shifted absorption of the in-falling atmosphere. Orange arrows are blue-shifted emission due to a blended inverse P Cygni profile.

Wallerstein 1982) who have found substantial disturbed profiles and large displacement from metallic lines.

In the star sample, blue-shifted H α emissions are observed in S Nor, S Mus and β Dor around $\phi = 0.5 - 0.6$ (see orange arrow in Fig. 3d). Since the atmosphere is in-falling at these phases for resonance stars, an inverse P Cygni profile could appear if the gas is high enough and reaches supersonic velocities as it is the case for short- and long-period cepheids.

In addition, S Nor and β Dor profiles are importantly wider around $\phi = 0.75 - 0.80$ (see Fig. 3d and Fig. B.11 respectively) with the appearance of a double absorption profile. These features are not observed on S Mus at phase $\phi=0.9$ and there is no phase coverage beyond $\phi = 0.5$ for ζ Gem. The red-shifted absorption in the profile (see red arrow in Fig. 3d) is caused by the infalling motion of the atmosphere while the blue-shifted absorption is likely due to the main shock produced by the κ mechanism in the star interior, which is later propagating outward in the star atmosphere. Then, we expect the collision between these in-falling layers and the main shock, which could result in a line enlargement feature around $\phi=0.8$.

3.3. Long-period cepheids $P > 10d$

For long-period Cepheids ($P > 10d$) we confirm the global atmosphere dynamics from H α profiles presented by Gillet (2014) in the case of X Cygni (16.3d). This author described three different H α stages per cycle which are in agreement with the UVES observations of the 10 long-period Cepheids presented in this paper:

1. From $\phi = 0.9$ to 0.3 when the photosphere is expanding, we observe the presence of a blue-shifted H α absorption (see blue arrows in Fig. 4d) which is identified as a gas flow at the

rear of the main shock due to κ -mechanism when emerging from the photosphere at $\phi \approx 0.85$ (see blue zone in Fig. 6a). This feature is accompanied by a red-shifted absorption due to the infalling atmosphere layers.

2. Between phase 0.9 and 0.5, a P Cygni profile is observed (see green arrows in Fig. 4d). This P Cygni profile is interpreted as H α emission at the rear of the main shock front propagating outward. It appears as a P Cygni profile when it is sufficiently detached from the photosphere (see green zone in Fig. 6a). This feature progressively disappears between $\phi = 0.3$ to 0.6 and is no longer visible around $\phi \approx 0.6$ (see Figs. 4d and 6b).
3. From $\phi = 0.7$ to 0.9 a double absorption profile appears with a blue-shifted emission. This double absorption is composed of an absorption centered on the stellar rest frame and a red-shifted absorption at $\approx 50\text{km/s}$. The motionless absorption feature have been attributed to a CSE by several authors, not only in the case of ℓ Car (Rodgers & Bell 1968; Baldry et al. 1997; Nardetto et al. 2008), but also in the case of the Type II long-period Cepheid W Virginis (Kovtyukh et al. 2011). On the other hand, the red-shifted absorption is due to hydrogen in-falling layers during the ballistic motion. As a result, the blue-shifted emission (orange arrows in Fig. 4d) is a blend between an inverse P Cygni profile caused by the supersonic infalling layers, and both a photospheric and a CSE absorption (see Figure 5b).
4. From $\phi = 0.9$ to 1.0 the inverse P Cygni profile progressively disappears. Two effects could contribute together to explain this transition. First, since the layers are infalling, at a certain point they are not high enough in the atmosphere to produce a P Cygni profile. Secondly, the main shock emerges from the photosphere at phase $\phi \approx 0.85$, then a blue-shifted absorption could progressively blends the P Cygni emission.

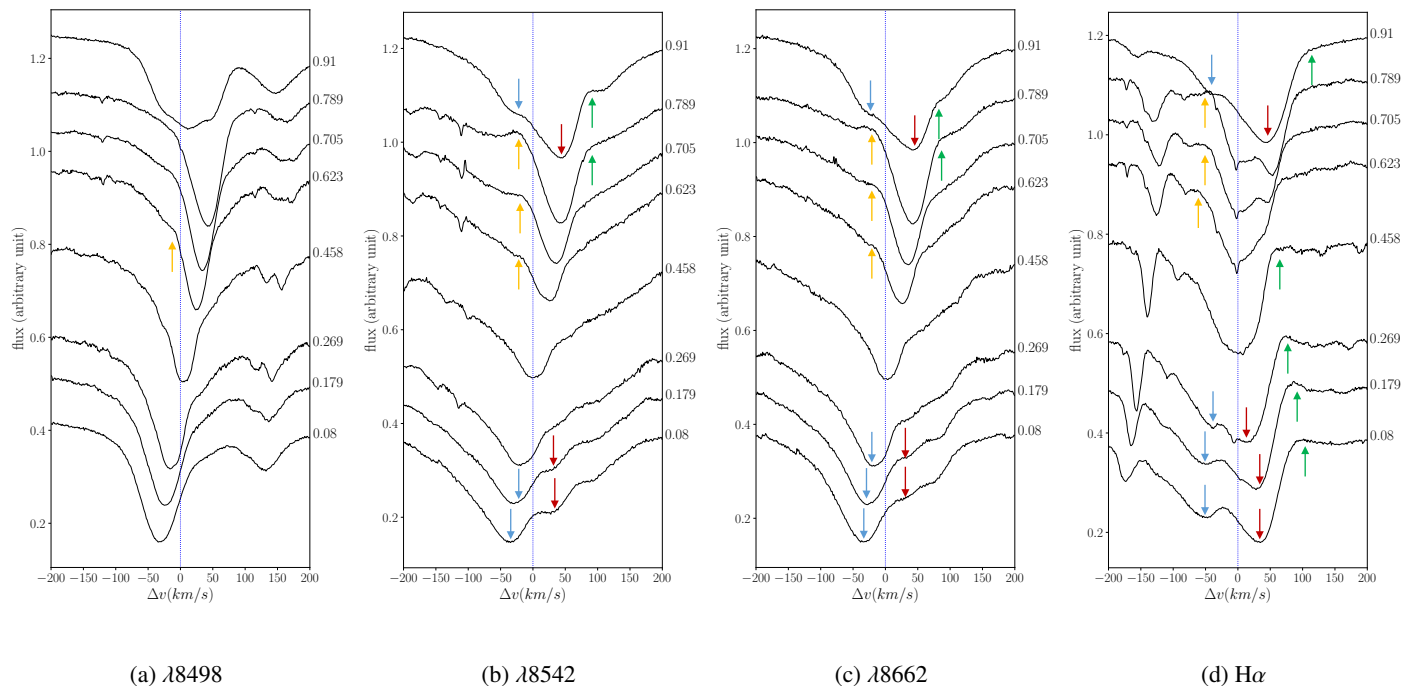


Fig. 4: VZ Pup, 23.17d. Blue arrows are blue-shifted absorption due to the main shock. Red arrows are red-shifted absorption of the in-falling atmosphere. Green arrows are red-shifted emission due to a P Cygni profile. Orange arrows are blue-shifted emission due to an inverse P Cygni profile.

4. Ca IR profile variations

In this section, we qualitatively describe and physically interpret Ca IR profile variations. We further show that Ca IR profile features are similar to $H\alpha$ profile variations since they are induced by the same phenomena. We synthesized our findings in Fig. 6 and Table 2.

4.1. Short-period cepheids $P < 10d$

Similarly to $H\alpha$ lines presented in Sect 3.1, Ca IR profiles are almost quiescent during the pulsation cycle. However, a finer inspection reveals a weak blue-shifted emission between $\phi \approx 0.6 - 0.9$ which is always synchronized with $H\alpha$ blue-shifted emission (see orange arrows in Fig. 2). Hence, we can infer that Ca IR blue-shifted emission has the same origin same origin as a $H\alpha$, the in-falling upper atmosphere layers are causing a radiative shock, resulting in an inverse P Cygni profile. The line $\lambda 8498$ is less disturbed than the two others lines, a result that we find also for medium and long-period Cepheids. According to [Linsky et al. \(1970\)](#) this line is formed lower in the chromosphere than the two others, as a result, the acceleration is less important during ballistic movement of the atmosphere for line $\lambda 8498$ and could not be high enough in the atmosphere to produce a P Cygni profile.

4.2. Medium-period cepheids $P \approx 10d$

In the case of medium-period Cepheids we also find the two profile features identified in the case of $H\alpha$ profiles, that is a blue-shifted emission followed by an enlargement of the lines (see Figs. 3b and 3c). However in this case it is less clear if we

observe a simple enlargement due to turbulence or a double absorption profile which would be not resolved. Indeed, medium-period Cepheids are an intermediate case between short-period Cepheids which are dominated by the turbulence during the in-falling motion, and a double absorption profile as it is the case in long-period Cepheids.

4.3. Long-period cepheids $P > 10d$

For all the profile variations presented in this paper we report the following Ca IR profile sequence over the pulsation period:

1. From $\phi = 0.9$ to 0.3 there are two important spectral features. First, we observe a double absorption profile centered on 0 km/s velocity. The same features were recently observed by [Wallerstein et al. \(2019\)](#) who published Ca IR profiles of X Cygni with a good phase coverage. We interpret this feature as a Schwarzschild mechanism ([Schwarzschild 1952](#)). Briefly, this phenomenon can be produced when two layers of an atmosphere with an opposite velocity field are colliding on each other. In the present case it is caused by the collision between the main shock expanding outward and the lower chromosphere region descending toward the photosphere (see Fig. 6a). Thus, both a blue- and a red-shifted absorption component symmetrically centered on the stellar restframe are observed (see blue and red arrows respectively in Figs. 4b and 4c). This phenomenon is weaker or absent for the line $\lambda 8498$. We study in detail this behaviour in Sect. 6. Secondly, we also observe a red-shifted emission (see green arrows in Figs. 4b and 4c). We attributed this feature to a P Cygni profile due to the radiative wake at the rear of the

Table 2: Observational features of calcium infrared triplet in the star sample. The Table is divided into pulsation periods (columns) and phase interval (rows). In Fig. 6 we represent the mean features observed in each phase interval.

ϕ interval	Small (P<10d)	Medium (P \approx 10d)	Long (P>10d)
0.9-0.3	- Quiescent profiles: The atmospheric layers are moving outward.	- Quiescent profiles	- Schwarzschild mechanism: In-falling chromosphere layers are collapsing onto the emerging shock causing a double absorption profile - P Cygni profile: The main shock front is still propagating and progressively leaves Ca IR layers, entering in outermost H α layers.
0.3-0.6	- Quiescent profiles	- Inverse P Cygni profile: Emission from supersonic infalling layers.	- Quiescent profiles
0.6-1.0	- Inverse P Cygni profile: A weak emission is observable in several short-periods - Profile enlargement: The profiles are importantly wider due to turbulences during atmosphere collision.	- Line doubling: Enlargement of the line profile which is possibly a double profile due to a Schwarzschild scenario.	- P Cygni profile: It appears when the main shock from the previous cycle is high enough in the chromosphere. - Inverse P Cygni profile: Emission from supersonic infalling layers. - Transition phase: From 0.9 to 1.0 the latter emission progressively disappears. Schwarzschild mechanism initiates.

main shock (initiated at the end of the previous cycle) which is still propagating outward.

- From $\phi = 0.3$ to 0.6 the main shock has reversed the atmosphere movement which is now expanding. The main shock continues to propagate, as shown in Fig. 6b and all Ca IR profiles are passing through a quiescent phase. No particular features are observed.
- Between $\phi = 0.6$ and 0.9 a blue-shifted emission is observed (see orange arrows in Figs. 4a to 4c). In the case of VZ Pup this emission is seen from $\phi=0.623$ to 0.789 with an increasing intensity, which is almost 20% of the pulsation cycle. Similarly to H α , we attribute this feature to an inverse P Cygni profile due to the supersonic in-falling movement of the atmosphere (see Fig. 6c). However, contrary to H α it is not a double absorption profile. Indeed since the abundance of calcium is lower than hydrogen, we expect a weaker CSE absorption from Ca IR in long-period Cepheids. We suggest it could contribute enough in some cases to blend a part of the Ca IR emission as it is the case in the sample for U Car and ℓ Car in Figs. B.18 and B.19.

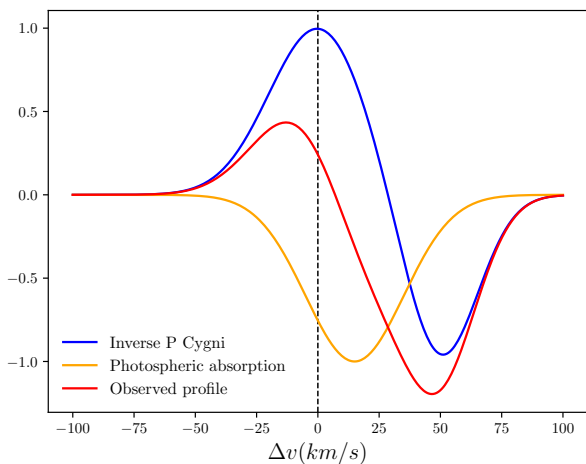
As a conclusion from the analysis of the Ca IR profiles in the entire star sample, the presence of Ca IR emissions indicate a chromospheric activity in the Cepheid upper atmosphere (Busà et al. 2007). Hence, the chromosphere is activated either by shocks during the infalling movement of the atmosphere or by the main shock propagating outward. In case of long-period Cepheids this emission is also observed for a significant part of the pulsation cycle ($\Delta\phi \approx 0.2$).

5. Chromosphere kinematics using Van Hoof effect

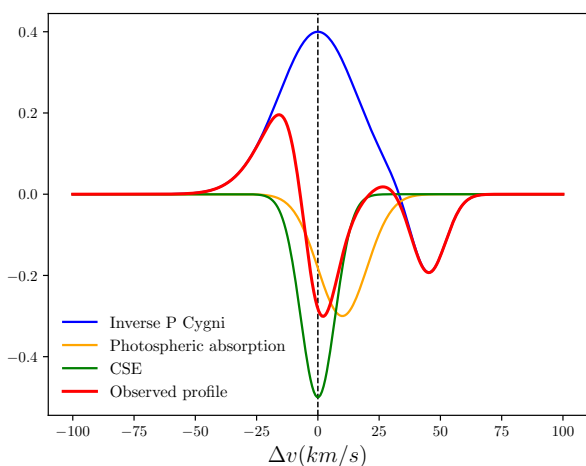
By studying solar chromosphere, Vernazza et al. (1973) derived a H α core formation height higher than Ca IR. In addition, ac-

ording to Linsky et al. (1970), the core of Ca λ 8498 is formed lower than the other calcium lines in the chromosphere. Hence, by comparing Ca λ 8498 and H α core formation layers from Cepheids, we expect to directly obtain information on the velocity gradient between the bottom and the top of the chromosphere. In order to study the motion of the chromospheric layers we derive heliocentric RVs curves of Ca λ 8498 and H α by measuring the minimum of the line. Therefore, we probe the RV associated to the core-forming region. When a double profile absorption is observed, as it is the case in VZ Pup, we consider only the red-shifted absorption since it is produced by the atmospheric layers. We present the results in Fig. 7.

From these figures, H α line and Ca λ 8498 are well synchronized in the case of the short-period AX Cir, whereas the variation of H α is late respected to Ca λ 8498 in S Nor and VZ Pup. This de-synchronization is similar to the Van Hoof effect (van Hoof & Struve 1953) in the case of hydrogen and metallic lines. This phenomenon is interpreted as an outward propagating wave all along the pulsation cycle (Mathias & Gillet 1993). We demonstrate the global de-synchronization of the chromospheric layers due to the propagation of waves for mid- and long-period Cepheids. Acceleration of Ca IR and H α are almost identical in the case of AX Cir, which is likely a sign of a compact chromosphere due to the higher gravity field in short-period Cepheids. For both S Nor and VZ Pup we observe an in-falling movement which accelerates up to about 30km/s. Then, a sudden reverse from in-falling (> 0 km/s) to outward motion (< 0 km/s) is observed around 0.7 in case of S Nor while it appears later for VZ Pup at $\phi \approx 0.9$. For long-period Cepheids we can hypothesize that reversal motion of the atmosphere occurs later due to larger ballistic motion in Cepheids of lower gravity field. Then, Ca IR lines reverse first their movement followed



(a) Inverse P Cygni blended with photosphere



(b) Inverse P Cygni blended with CSE + photosphere

Fig. 5: Schematic profile formation of a blended inverse P Cygni profile. (a) The supersonic (≈ 50 km/s) descending atmospheric layers produce a radiative emission centered on 0 km/s (blue curve). This profile is blended with photospheric red-shifted (≈ 15 km/s) absorption (orange curve) resulting in an apparent weak blue-shifted emission. (b) In long-period Cepheids a component centered on 0 km/s is attributed to a CSE (green) and causes the appearance of a double absorption profile.

by $H\alpha$ lines (see red and blue curves in Fig. 7). The larger de-synchronization for longer period Cepheids is likely responsible of the Schwarzschild mechanism in Ca IR that we study in next Sect. 6.

In order to explore the link between period of Cepheids and upper atmosphere de-synchronization in the entire star sample, we derive the norm of the velocity gradient between Ca IR and $H\alpha$ spectral lines, averaged over the pulsation cycle:

$$\Delta v = \frac{1}{N} \sum_{i=1}^N |V_{\lambda 8498}(\phi_i) - V_{H\alpha}(\phi_i)| \quad (1)$$

where $V_{\lambda 8498}$ and $V_{H\alpha}$ are radial velocities of Ca IR and $H\alpha$ measured using the minimum of the line profile, and N is the total

number of pulsation phase. We also adopted the standard error of the mean s for N epoch in a pulsation cycle:

$$s = \frac{\sigma(\Delta v)}{\sqrt{N}} \quad (2)$$

where $\sigma(\Delta v)$ is the standard deviation of the mean. The result is presented in Fig. 8.

Since the pulsation cycle coverage is relatively poor in the star sample, the Δv quantity (Eq. 1) do not cover the full pulsation cycle and depends on the specific phases of observation. However, from Fig. 8 we can clearly observe a tendency with two distinct regimes:

1. For Cepheids with period $P < 10$ d, the layers associated to the top of line-forming regions of Ca IR and $H\alpha$, respectively, are synchronized (with $\Delta v < 5$ km/s.)
2. A sudden increase appears for $P \approx 10$ d with a velocity gradient of the $H\alpha$ layer compared to Ca IR rising up to 30 km/s.

6. The size of the chromosphere estimated from the Schwarzschild mechanism of long period Cepheids

We observe the Schwarzschild phenomenon for 8 out of 10 long-period Cepheids (Schwarzschild 1952) between $\phi=0.9$ and 0.3. Indeed, the observed profiles follow the classical picture of the Schwarzschild scenario in which the center-of-mass velocity falls in between the blue and red peaks. Moreover, since Linsky et al. (1970) found that Ca $\lambda 8498$ line is formed lower in the chromosphere than Ca $\lambda 8542$ and $\lambda 8662$ spectral lines, we can infer that Ca $\lambda 8498$ line is colliding first onto the main shock, which is confirmed by the fact that Ca $\lambda 8498$ line is always in a more advanced stage in the Schwarzschild scenario than Ca $\lambda 8542$ and $\lambda 8662$ lines, respectively (see for example Fig. 4). Although we cannot firmly conclude because of possible cycle-to-cycle variation effects (Anderson 2016), the Schwarzschild mechanism could be a common feature in long-period Cepheids.

The Schwarzschild mechanism itself occurs during the expansion of the Cepheids photosphere around $\phi=0.9$. It is explained by a collision between the in-falling layers of the lower chromosphere on denser region of the ascending photosphere. For each long-period Cepheids presenting double line features we derive RVs from both blue-shifted V_{blue} and red-shifted V_{red} components using a bi-Gaussian fitting. We provide an example of this fitting in Fig. 9. From this fitting we obtain both mean and standard deviation values of blue and red absorption components. We also estimate the shock amplitude, by simply assuming $A_{\text{shock}} = V_{\text{red}} - V_{\text{blue}}$ and constant velocities during the in-falling motion. Results are presented in Table A.1.

We obtain shock amplitudes between 50 and 80 km/s. Although these profiles belong to different pulsation phases we observe no trend between the shock amplitude and the period of the Cepheids. In the case of VZ Pup the Schwarzschild mechanism is initiated at the end of the pulsation cycle ($\phi = 0.91$) for Ca $\lambda 8542$ and $\lambda 8662$. The double line feature disappears after $\phi=0.179$. In that case, it took at least a quarter cycle ($\Delta\phi \approx 0.250$) for Ca $\lambda 8542$ and $\lambda 8662$ layers to collapse entirely on the photospheric denser region, resulting in a single blue-shifted component. If we assume a constant shock amplitude during the collapsing of the chromosphere, we can approximate the maximum height of Ca $\lambda 8542$ and $\lambda 8662$ core formation regions. Indeed this is simply the atmosphere distance covered in

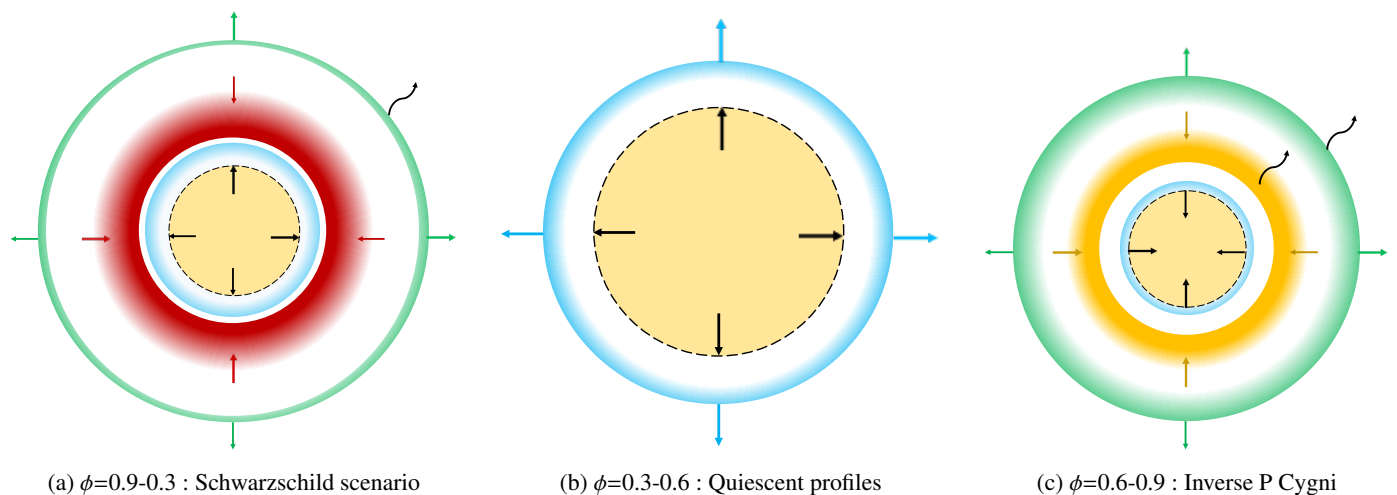


Fig. 6: General scheme of the pulsating chromosphere dynamics from Ca IR variations. **(a)** As the main shock continue to propagate outward causing a radiative wake (black arrow emitted by the green zone), H α exhibits a blended P Cygni profile. At the same time a blue-shifted absorption appears from the emerging main shock from the κ mechanism (blue zone). This shock collides the Ca IR in-falling layers (red zone) which produces a Schwarzschild profile (Sect. 6). **(b)** Quiescent phase: The main shock has reversed the movement of the atmosphere which is now entirely propagating outward. H α P Cygni profile progressively disappears around $\phi=0.5$. **(c)** Following a ballistic motion, layers of the atmosphere fall on the star (orange area). Supersonic velocities are reached if the acceleration is strong enough and thus an inverse P Cygni profile appears for H α , Ca $\lambda 8542$ and $\lambda 8662$. The main shock continues to propagate outward and a Ca IR P Cygni profile could appear due to a radiative wake emission from chromosphere (black arrow emitted by the green zone)

Table 3: Chromospheric radius R_{chromo} estimated from shock amplitude listed in Table A.1 in the case of the calcium line $\lambda 8542$. R_{chromo} is given relatively to the mean stellar radius provided by PR relation from Gallenne et al. (2017)¹. Calculation assumes $\Delta\phi = 0.250$ for Schwarzschild mechanism duration.

Star	A_{shock} (km/s)	$R(R_{\odot})$	$R_{\text{chromo}}(\%R)$
TT Aql	82.9 \pm 1.1	82.0 \pm 1.0	43.2 \pm 1.1
RZ Vel	80.1 \pm 1.3	107.4 \pm 1.6	47.2 \pm 1.5
WZ Car	83.2 \pm 0.4	116.7 \pm 1.8	50.9 \pm 1.0
VZ Pup	69.3 \pm 0.6	117.2 \pm 1.8	42.5 \pm 1.0
T Mon	82.4 \pm 0.8	130.2 \pm 2.2	53.1 \pm 1.4
U Car	59.1 \pm 0.4	167.0 \pm 3.2	42.7 \pm 1.1
RS Pup	81.3 \pm 1.7	174.5 \pm 3.5	60.0 \pm 2.5
V1496 Aql	56.0 \pm 1.3	238.3 \pm 5.5	47.7 \pm 2.2

(1): Mean radius from PR relation:

$$\log R = (0.684 \pm 0.007)(\log P - 0.517) + (1.489 \pm 0.002)$$

a quarter period by the relative velocity of the collapsing layers $R_{\text{chromo}} = P\Delta\phi A_{\text{shock}}$. We thus estimate this distance assuming $\Delta\phi = 0.250$ and using the shock amplitude from Ca $\lambda 8542$ derived in Table A.1. In order to derive the chromospheric radius expressed by the mean stellar radius, we used the Period-Radius (PR) relation from Gallenne et al. (2017). Applying the same methodology for the long-period Cepheids in the sample, we find an extension for the chromosphere of Cepheids from about 40 to 50% of the mean stellar radius. The results are presented in Table 3. This order of magnitude is in agreement with (Wallerstein 1972) who estimated a Ca II fallen distance of 50% the radius of the star in the case of T Mon.

7. Discussion

7.1. Pulsating chromosphere as the origin of an ionized shell

A central question raised in the introduction is whether or not the pulsating chromosphere has the potential to ionize the gas in the environment to produce IR excess such as the one that would be caused by a shell of ionized gas, which represents 15% of the photosphere radius (Hocdé et al. 2020). In this paper, we studied the lower chromosphere of Cepheids for which we estimated a size to be at least 50% of the star radius.

Several processes are able to provide ionized material in the lower chromosphere. We have analyzed three episodes which have the potential to heat up and massively ionize the upper atmosphere: (1) the main shock traveling through the upper atmosphere whose front amplitude can reach 100km/s (2) a shock caused by supersonic descending layers of the atmosphere revealed under the form of an inverse P Cygni profile, and (3) a Schwarzschild mechanism caused by the main shock which is reversing the movement of the descending layers of the atmosphere.

However, according to shock theory (Fokin et al. 2000, 2004), shocks alone seem unlikely to provide a permanent free-free continuum which could explain a constant IR excess. These authors have shown that cooling by FeI and FeII lines in the post-shock region is more effective than cooling by free-free and bound-free continuum. Moreover these authors have also estimated a size of the post-shock region of about 100 km, and, given that shock velocities are 10 to 100 km/s, we deduce a cooling time of the order of tens of seconds which is short compared to a pulsation period.

Besides, the main shock traversing the photosphere rules a lot of processes in the behaviour of Cepheids. Indeed, it is already hypersonic when it emerges from the surface of the star, with a shock velocity of about 100 km/s or more, that is a Mach number between 10 and 20. In this case the convection zone

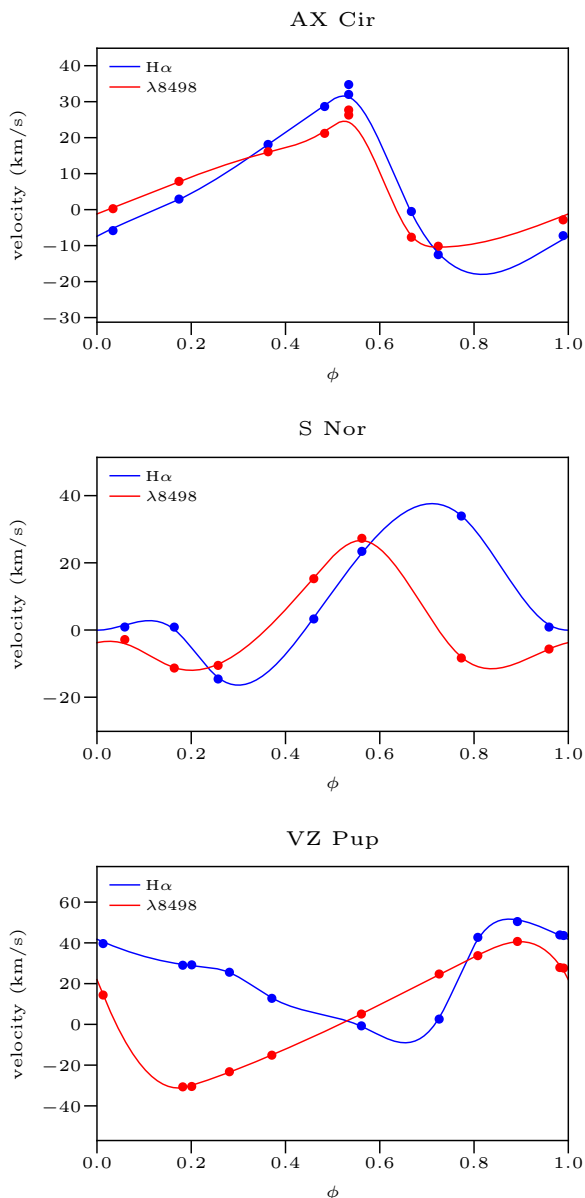


Fig. 7: Radial velocity of line Ca $\lambda 8498$ and $H\alpha$ line along the pulsation cycle ϕ for prototype stars. The solid curves are built from a spline fit to the RV data to guide the reader's eye.

could be strongly disrupted or inhibited at least for a fraction of the pulsation cycle. We propose, therefore, that this shock could be strong enough to bring hot and dense material in the upper atmosphere. Interestingly, Kraft (1957) also suggested that the transitory development from Ca II K emission in classical Cepheids is associated with the presence of hot material low in the atmosphere. He further discusses that this material could have been convected upward from hydrogen convection zone below the surface.

7.2. A plausible source of X-ray emission in the upper chromosphere

Another interesting question is to understand the origin of periodic X-ray emissions around phase $\phi=0.45$ at maximum radius that have been observed by Engle et al. (2017). Such X-

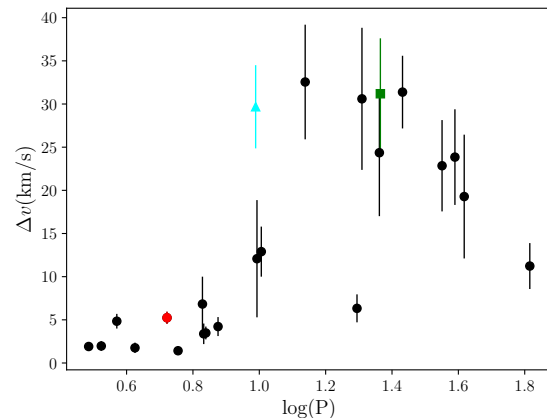


Fig. 8: Norm of the velocity gradient averaged over the pulsation cycle estimated using Eq (1) versus logarithm of the pulsation period. Red, cyan and green marks are AX Cir, S Nor and VZ Pup respectively.

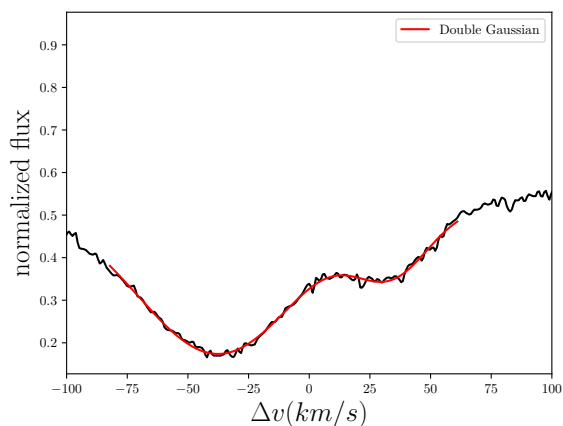


Fig. 9: Example of bi-Gaussian fit in the case of VZ Pup for line $\lambda 8542$ at the pulsation phase $\phi=0.08$. The parameters associated to the bi-Gaussian fits are listed for all stars in Table A.1, together with the derived shock amplitude.

ray emissions could stem from a high temperature plasma in the higher chromosphere. Indeed at this phase, the shock is well detached from the photosphere. When the P-Cygni appears in $H\alpha$ line at phase 0.0, the shock has already travelled $\approx 15\%$ of the photospheric radius with a speed of 100 km/s or more. Then, the shock decelerates below 100 km/s around $\phi=0.5$, thus the shock is no longer able to produce hydrogen emission. At this time, the shock traveled a distance close to the photospheric radius and is now propagating in the upper atmosphere where the density is 3 or 4 orders of magnitude weaker (10^{-11} - 10^{-12} g / cm^3) than that in the photosphere (10^{-8} g / cm^3). In this case, according to Fadeyev & Gillet (2004), with such pre-shock density in the upper atmosphere, the thickness of the radiative wake increases by almost 3 orders of magnitude while the temperature just after the shock front changes relatively little. Part of the thickness of the radiative shell will be a few or at least thousands of kilometers. The plasma behind the shock is also strongly compressed, proportional to the square of the Mach number (given by Hugoniot-Rankine equation in isothermal condition), and so does the amplification rate of the magnetic field, preexisting or generated by the plasma of the radiative wake, which may easily

reach a factor of 100. Therefore, in the upper chromosphere, part of the energy dissipation of the shock may be in non-collisional form. As a conclusion, we suggest that the energy producing X-ray flux between $\phi \approx 0.4$ - 0.5 could be deposited by the main shock in the outermost layers of the chromosphere.

7.3. Is the Gaia RVS sensitive to the chromosphere dynamics ?

The Gaia RVS has a narrow wavelength range centered on the Ca IR triplet (from ~ 845 to ~ 872 nm, see Sartoretti et al. 2018). Thus, we can expect the RV time series produced by the RVS to be dependent on the Ca IR behavior. From the chromosphere kinematics using Van Hoof effect in Sect. 5, we have shown that H α lines are de-synchronized with an important velocity gradient compared to Ca IR for Cepheids with pulsation period larger than about 10d. We therefore suggest that the same tendency as seen in Fig. 8 could appear between metallic lines (which is formed at a great optical depth) and Ca IR when observing with the RVS instrument. This de-synchronization between metallic and Ca IR lines was already observed by Wallerstein et al. (2015, 2019) for Cepheids δ Cep and X Cyg. Further investigations are necessary to quantify these differences and calibrate, if necessary, the projection factor to be used together with the RVS measurements of Cepheids radial velocities, in the Baade-Wesselink method of distance determination (Nardetto et al. 2017).

8. Conclusion

We analyzed H α and Ca IR profile variations to qualitatively describe the chromosphere dynamics over the pulsation period based on a sample of 24 stars with a good period coverage from short- up to long-period Cepheids. We demonstrate that Ca IR are interesting lines for probing dynamics in the lower chromosphere of Cepheids, complementary to H α lines, because their core probe different heights in the atmospheric layers, and it is an unambiguous indicator of chromospheric activity. Our analysis leads to the following conclusions:

1. We confirm the H α profile variation model made by Gillet (2014) in the particular case of X Cygni for a wider sample of long-period Cepheids.
2. As found by Nardetto et al. (2008), in the case of ℓ Car, we identified a H α absorption features centered on 0 km/s in at least 8 long-period Cepheids (TT Aql, RZ Vel, WZ Car, VZ Pup, T Mon, ℓ Car, U Car, RS Pup) that we interpret as a static CSEs which obscure the chromosphere and the star. Since the calcium abundance is lower than hydrogen, we expect that the CSE absorption is weaker in Ca IR compared to H α . However we do not exclude a possible blend of the calcium emissions if the CSE is denser in some cases.
3. We demonstrated that at least two mechanisms are pulsationally activating the chromosphere owing to Ca IR diagnostic: (1) An inverse P Cygni profile emission during supersonic in-falling motion and (2) a P Cygni profile emission due to the radiative wake behind the main shock when it is sufficiently detached from the photosphere. In addition, a blended emission during Schwarzschild mechanism is also not excluded due to large amount of kinetic energy to be released when the main shock and the in-falling atmosphere are colliding.
4. The difference in height formation of Ca IR and H α creates a de-synchronization of their associated chromospheric layers due to an outward propagation wave. We observe a weak phase delay and velocity gradient ($\Delta v < 5$ km/s) in small period Cepheids ($P < 10$ days) while H α lines are delayed with an important velocity gradient (up to $\Delta v \approx 30$ km/s) compared to Ca IR in mid- and long-period Cepheids.
5. This de-synchronization in long-period Cepheids is likely responsible for the Schwarzschild mechanism of Ca IR lines during the beginning of photosphere ascending phase from $\phi=0.9$ to 0.3. This phenomenon is possibly a common feature since we observed this feature among 8 out of 10 long-periods. The collision velocity between in-falling layers of the lower part of the atmosphere and the photospheric region is about 50 up to 80km/s. Since the in-falling motion lasts for at least a quarter cycle we derived the height of Ca IR core formation to be $\approx 50\%$ of the star radius in long-period Cepheids, which is consistent at the first order with the size of the shell of ionized gas (15% of the stellar radius) found by Hocdé et al. (2020).

References

- Anderson, R. I. 2016, MNRAS, 463, 1707
- Astropy Collaboration, Price-Whelan, A. M., Sipőcz, B. M., et al. 2018, AJ, 156, 123
- Baldry, I. K., Taylor, M. M., Bedding, T. R., & Booth, A. J. 1997, MNRAS, 289, 979
- Bell, R. A. & Rodgers, A. W. 1967, MNRAS, 135, 121
- Berdnikov, L. N., Samus, N. N., Antipin, S. V., et al. 2004, PASP, 116, 536
- Bohm-Vitense, E. & Parsons, S. B. 1983, ApJ, 266, 171
- Borgniet, S., Kervella, P., Nardetto, N., et al. 2019, A&A, 631, A37
- Breitfelder, J., Mérand, A., Kervella, P., et al. 2016, A&A, 587, A117
- Breitfellner, M. G. & Gillet, D. 1993a, A&A, 277, 524
- Breitfellner, M. G. & Gillet, D. 1993b, A&A, 277, 553
- Breitfellner, M. G. & Gillet, D. 1993c, A&A, 277, 541
- Busà, I., Aznar Cuadrado, R., Terranegra, L., Andretta, V., & Gomez, M. T. 2007, A&A, 466, 1089
- Cauzzi, G., Reardon, K., Rutten, R. J., Tritschler, A., & Uitenbroek, H. 2009, A&A, 503, 577
- Cauzzi, G., Reardon, K. P., Uitenbroek, H., et al. 2008, A&A, 480, 515
- Chmielewski, Y. 2000, A&A, 353, 666
- Dekker, H., D’Odorico, S., Kaufer, A., Delabre, B., & Kotzlowski, H. 2000, in Proc. SPIE, Vol. 4008, Optical and IR Telescope Instrumentation and Detectors, ed. M. Iye & A. F. Moorwood, 534–545
- Engle, S. G., Guinan, E. F., Harper, G. M., et al. 2017, ApJ, 838, 67
- Fadeyev, Y. A. & Gillet, D. 2004, A&A, 420, 423
- Foing, B. H., Crivellari, L., Vladilo, G., Rebolo, R., & Beckman, J. E. 1989, A&AS, 80, 189
- Fokin, A., Massacrier, G., & Gillet, D. 2000, A&A, 355, 668
- Fokin, A. B. 1991, MNRAS, 250, 258
- Fokin, A. B., Gillet, D., & Breitfellner, M. G. 1996, A&A, 307, 503
- Fokin, A. B., Massacrier, G., & Gillet, D. 2004, A&A, 420, 1047
- Gaia Collaboration. 2018, VizieR Online Data Catalog, I/345
- Gallenne, A., Kervella, P., & Mérand, A. 2012, A&A, 538, A24
- Gallenne, A., Kervella, P., Mérand, A., et al. 2017, A&A, 608, A18
- Gallenne, A., Mérand, A., Kervella, P., et al. 2013, A&A, 558, A140
- Gillet, D. 2014, A&A, 568, A72
- Gontcharov, G. A. 2006, Astronomy Letters, 32, 759
- Groenewegen, M. A. T. 2020, A&A, 635, A33
- Hertzsprung, E. 1926, Bull. Astron. Inst. Netherlands, 3, 115
- Hocdé, V., Nardetto, N., Lagadec, E., et al. 2020, A&A, 633, A47
- Hubble, E. 1929, Proceedings of the National Academy of Science, 15, 168
- Hubble, E. P. 1926, ApJ, 64
- Jacobsen, T. S. & Wallerstein, G. 1981, PASP, 93, 481
- Jacobsen, T. S. & Wallerstein, G. 1982, PASP, 94, 471
- Katz, D., Sartoretti, P., Cropper, M., et al. 2019, A&A, 622, A205
- Kervella, P., Mérand, A., Perrin, G., & Coudé du Foresto, V. 2006, A&A, 448, 623
- Kervella, P., Trahin, B., Bond, H. E., et al. 2017, A&A, 600, A127
- Kovacs, G., Kisvarsanyi, E. G., & Buchler, J. R. 1990, ApJ, 351, 606
- Kovtyukh, V. V., Wallerstein, G., Andrievsky, S. M., et al. 2011, A&A, 526, A116
- Kraft, R. P. 1957, ApJ, 125, 336
- Leavitt, H. S. 1908, Annals of Harvard College Observatory, 60, 87
- Linsky, J. L., Hunten, D. M., Sowell, R., Glackin, D. L., & Kelch, W. L. 1979, ApJS, 41, 481
- Linsky, J. L., Teske, R. G., & Wilkinson, C. W. 1970, Sol. Phys., 11, 374
- Martin, J., Fuhrmeister, B., Mittag, M., et al. 2017, A&A, 605, A113

- Mathias, P. & Gillet, D. 1993, A&A, 278, 511
- Mérand, A., Kervella, P., Breitfelder, J., et al. 2015, A&A, 584, A80
- Mérand, A., Kervella, P., Coudé du Foresto, V., et al. 2006, A&A, 453, 155
- Mermilliod, J. C., Mayor, M., & Udry, S. 2008, A&A, 485, 303
- Munari, U. 1999, Baltic Astronomy, 8, 73
- Nardetto, N., Groh, J. H., Kraus, S., Millour, F., & Gillet, D. 2008, A&A, 489, 1263
- Nardetto, N., Poretti, E., Rainer, M., et al. 2017, A&A, 597, A73
- Pourbaix, D., Tokovinin, A. A., Batten, A. H., et al. 2004, A&A, 424, 727
- Reardon, K. P., Uitenbroek, H., & Cauzzi, G. 2009, A&A, 500, 1239
- Riess, A. G., Casertano, S., Yuan, W., Macri, L. M., & Scolnic, D. 2019, ApJ, 876, 85
- Riess, A. G., Filippenko, A. V., Challis, P., et al. 1998, AJ, 116, 1009
- Rodgers, A. W. & Bell, R. A. 1968, MNRAS, 138, 23
- Samus', N. N., Kazarovets, E. V., Durlevich, O. V., Kireeva, N. N., & Pastukhova, E. N. 2017, Astronomy Reports, 61, 80
- Sartoretti, P., Katz, D., Cropper, M., et al. 2018, A&A, 616, A6
- Sasselov, D. D. & Lester, J. B. 1994a, ApJ, 423, 795
- Sasselov, D. D. & Lester, J. B. 1994b, ApJ, 423, 777
- Sasselov, D. D. & Lester, J. B. 1994c, ApJ, 423, 785
- Schmidt, E. G. 1970, ApJ, 162, 871
- Schmidt, E. G. 2015, ApJ, 813, 29
- Schmidt, E. G. & Parsons, S. B. 1982, ApJS, 48, 185
- Schmidt, E. G. & Parsons, S. B. 1984, ApJ, 279, 202
- Schmidt, E. G. & Weiler, E. J. 1979, AJ, 84, 231
- Schwarzschild, M. 1952, In: Oosterhoff P.T. (ed.) Transactions of the IAU Vol. VIII, Cambridge University Press, 81
- Turner, D. G., Abdel-Sabour Abdel-Latif, M., & Berdnikov, L. N. 2006, PASP, 118, 410
- van Hoof, A. & Struve, O. 1953, PASP, 65, 158
- Vecchio, A., Cauzzi, G., & Reardon, K. P. 2009, A&A, 494, 269
- Vernazza, J. E., Avrett, E. H., & Loeser, R. 1973, ApJ, 184, 605
- Wallerstein, G. 1972, PASP, 84, 656
- Wallerstein, G., Albright, M. B., & Ritchey, A. M. 2015, PASP, 127, 503
- Wallerstein, G., Anderson, R. I., Farrell, E. M., et al. 2019, PASP, 131, 094203
- Watson, C. L., Henden, A. A., & Price, A. 2006, Society for Astronomical Sciences Annual Symposium, 25, 47
- Wilson, O. C. & Vainu Bappu, M. K. 1957, ApJ, 125, 661

Acknowledgements. The authors acknowledge the support of the French Agence Nationale de la Recherche (ANR), under grant ANR-15-CE31-0012-01 (project UnlockCepheids). We acknowledge financial support from “Programme National de Physique Stellaire” (PNPS) of CNRS/INSU, France. This project was partially supported by the Polish Ministry of Science grant Ideas Plus. This research made use of the SIMBAD and VIZIER³ databases at CDS, Strasbourg (France) and the electronic bibliography maintained by the NASA/ADS system. This research also made use of Astropy, a community-developed core Python package for Astronomy (Astropy Collaboration et al. 2018). This research has made use of the SIMBAD database, operated at CDS, Strasbourg, France. Based on observations made with ESO telescopes at Paranal La Silla observatories under program IDs: 098.D-0379(A), 0100.D-0397(A) and 0101.D-0551(A).

³ Available at <http://cdsweb.u-strasbg.fr/>

**Appendix A: Results of bi-Gaussian fitting for
Schwarzschild mechanism**

Appendix B: Calcium triplet of Cepheids with UVES

Table A.1: RVs fields in Schwarzschild mechanism in long-period Cepheids. Velocities were calculated only when the characteristic W-shape was clearly identified by-eye. In the third column of the table, lines 1,2 and 3 refer to Ca λ 8498, 8542 and 8662, respectively. V_{blue} , V_{red} are the blue and the red component velocities respectively of the W shape. A_{shock} is the shock amplitude derived by $V_{\text{blue}} - V_{\text{red}}$. The FWHM of blue (σ_{blue}) and red (σ_{red}) components are also listed. All values are given in (km/s). Stars are ranked by increasing periods from top to bottom.

Star	Phase	line	V_{blue}	V_{red}	A_{shock}	σ_{blue}	σ_{red}
TT Aql	0.947	2	-36.7±1.0	+46.2±0.5	82.9±1.1	42.8±0.9	31.6±0.7
		3	-29.7±0.7	+47.4±0.6	77.1±0.9	42.5±0.7	29.2±0.6
	0.116	2	-35.5±0.1	+41.7±0.7	77.2±0.7	41.4±0.7	15.1±0.8
		3	-31.6±0.1	+44.7±1.2	76.3±1.2	36.1±0.9	14.2±1.4
RZ Vel	0.955	2	-43.3±1.2	+36.8±0.6	80.1±1.3	35.0±0.8	18.5±0.6
		3	-40.0±0.1	+39.1±0.4	79.1±0.4	33.6±0.2	20.4±0.4
WZ Car	0.080	1	-43.0±0.1	+39.3±0.7	82.3±0.7	36.3±0.1	21.7±0.6
		2	-48.2±0.2	+35.0±0.4	83.2±0.4	34.3±0.8	31.6±0.4
		3	-46.2±0.1	+34.5±0.2	80.7±0.2	29.6±0.4	19.8±0.3
VZ Pup	0.080	2	-37.3±0.1	+32.0±0.6	69.3±0.6	29.8±0.7	14.0±0.8
		3	-34.2±0.1	+33.6±1.1	67.8±1.1	28.5±0.3	14.2±0.5
	0.179	2	-28.9±0.1	+32.3±0.4	61.2±0.4	29.4±0.3	10.5±0.5
		3	-26.6±0.1	+37.2±0.4	63.8±0.4	28.0±0.2	11.0±0.5
T Mon	0.123	1	-41.6±0.1	+28.2±0.7	69.8±0.8	35.7±1.1	16.0±0.5
		2	-49.4±0.2	+33.0±0.8	82.4±0.8	47.5±2.0	22.5±0.6
		3	-45.8±0.1	+28.6±0.1	74.4±0.1	36.0±0.3	17.4±0.1
U Car	0.197	2	-30.9±0.1	+28.2±0.1	59.1±0.4	30.1±0.5	17.3±0.5
		3	-26.8±0.1	+41.5±2.9	68.3±2.9	20.3±0.3	6.5±1.6
	0.225	2	-27.1±0.2	+33.6±1.6	60.7±1.6	37.0±1.2	16.5±0.5
		3	-24.5±0.2	+40.6±0.1	65.1±0.2	37.8±2.3	18.0±0.9
RS Pup	0.280	1	-33.6±0.1	+30.4±0.7	64.0±0.7	33.1±1.3	14.8±0.5
		2	-41.1±1.0	+40.2±1.4	81.3±1.7	54.1±3.6	26.4±1.8
		3	-36.1±0.9	+35.9±0.7	72.0±1.1	44.0±1.5	20.2±0.4
V1496 Aql	0.625	1	-20.7±0.3	+28.5±0.3	49.2±0.4	17.2±0.4	21.6±0.3
		2	-38.5±1.2	+32.8±0.4	71.3±1.3	28.1±0.6	32.5±1.2
		3	-27.2±0.7	+33.4±0.4	60.6±0.8	26.2±0.8	24.9±0.6

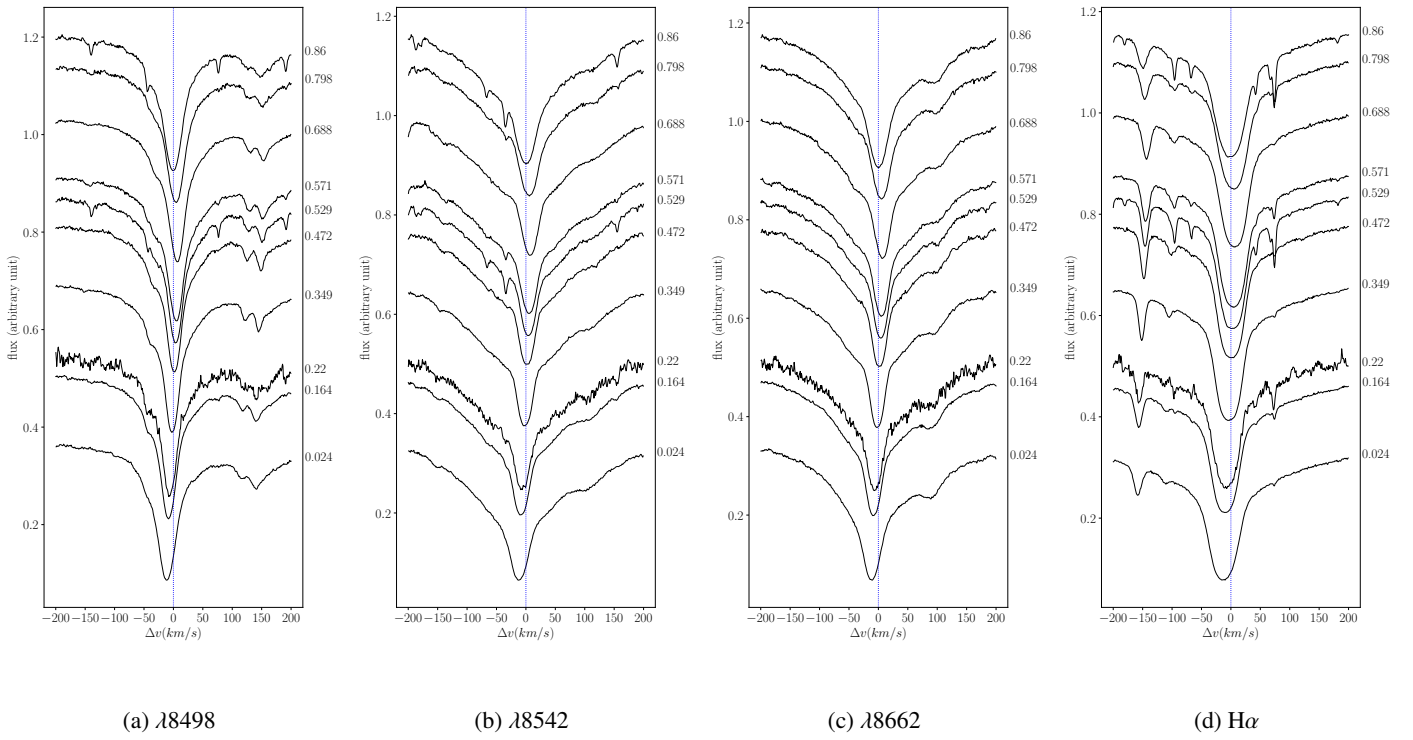


Fig. B.1: AV Cir, 3.06d

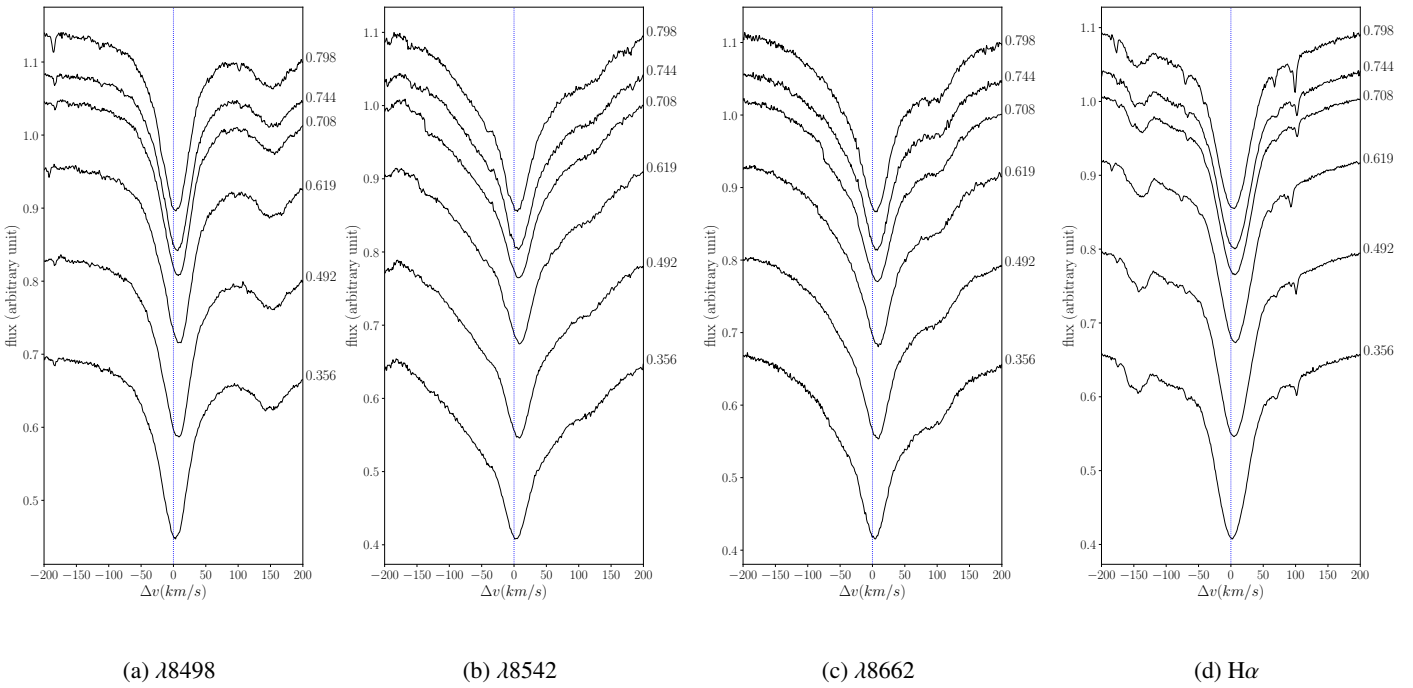


Fig. B.2: BG Cru, 3.34d

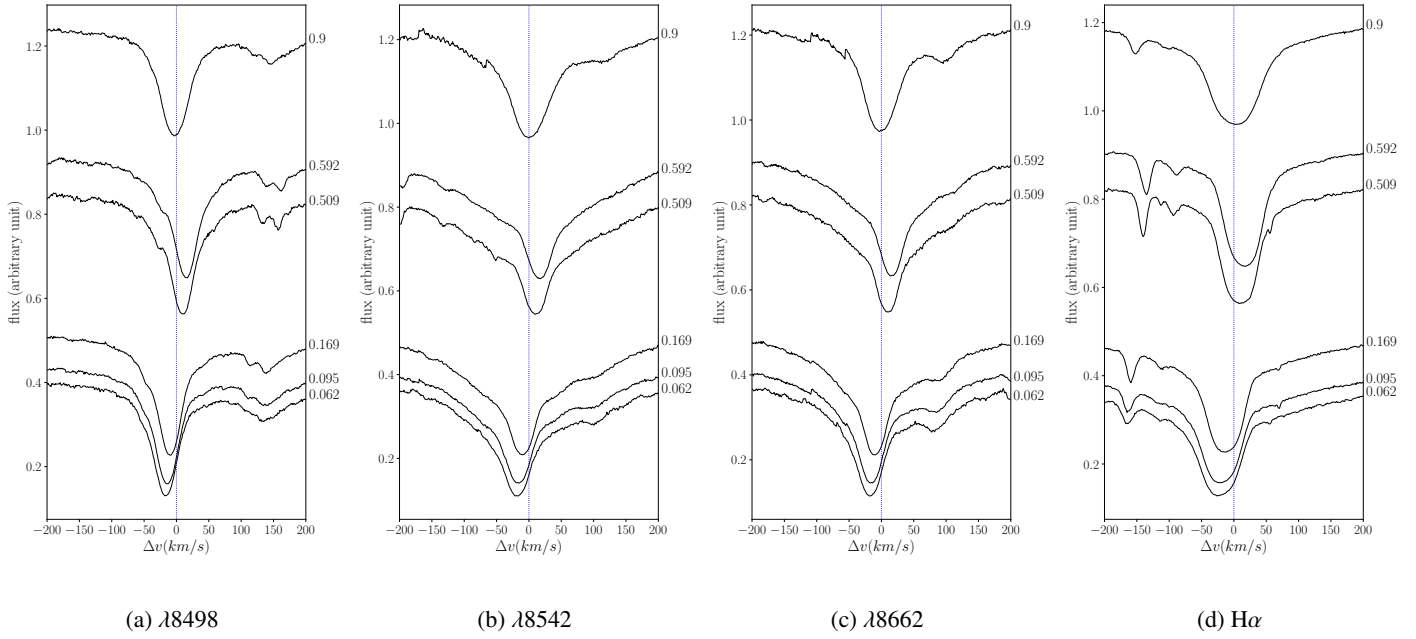


Fig. B.3: RT Aur, 3.74d

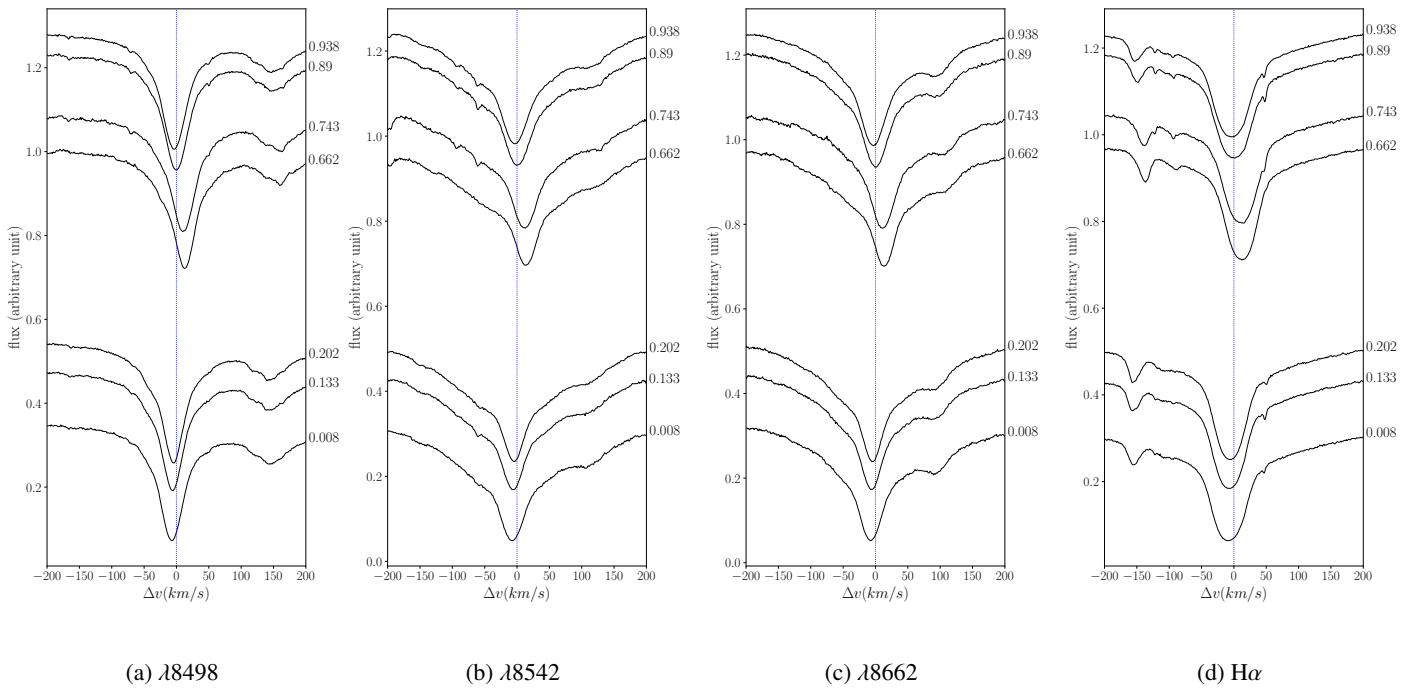


Fig. B.4: AH Vel, 4.22d

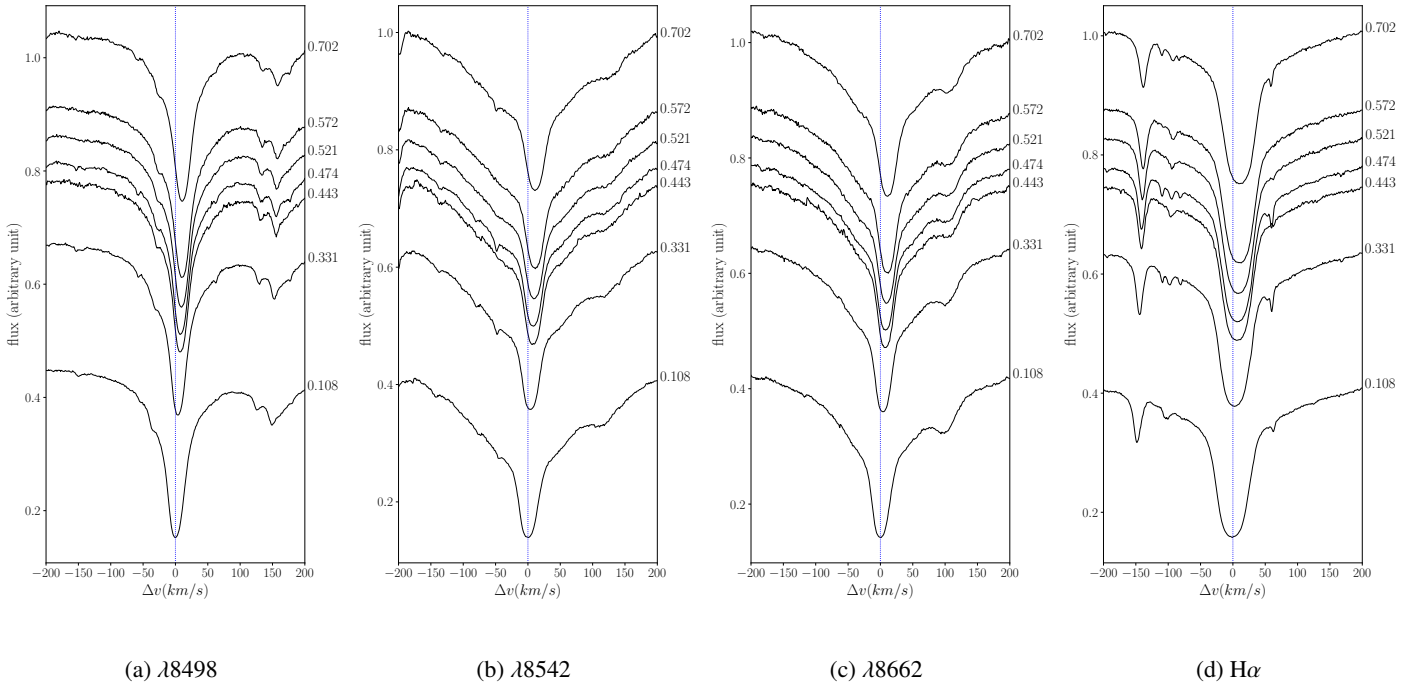


Fig. B.5: MY Pup, 5.69d

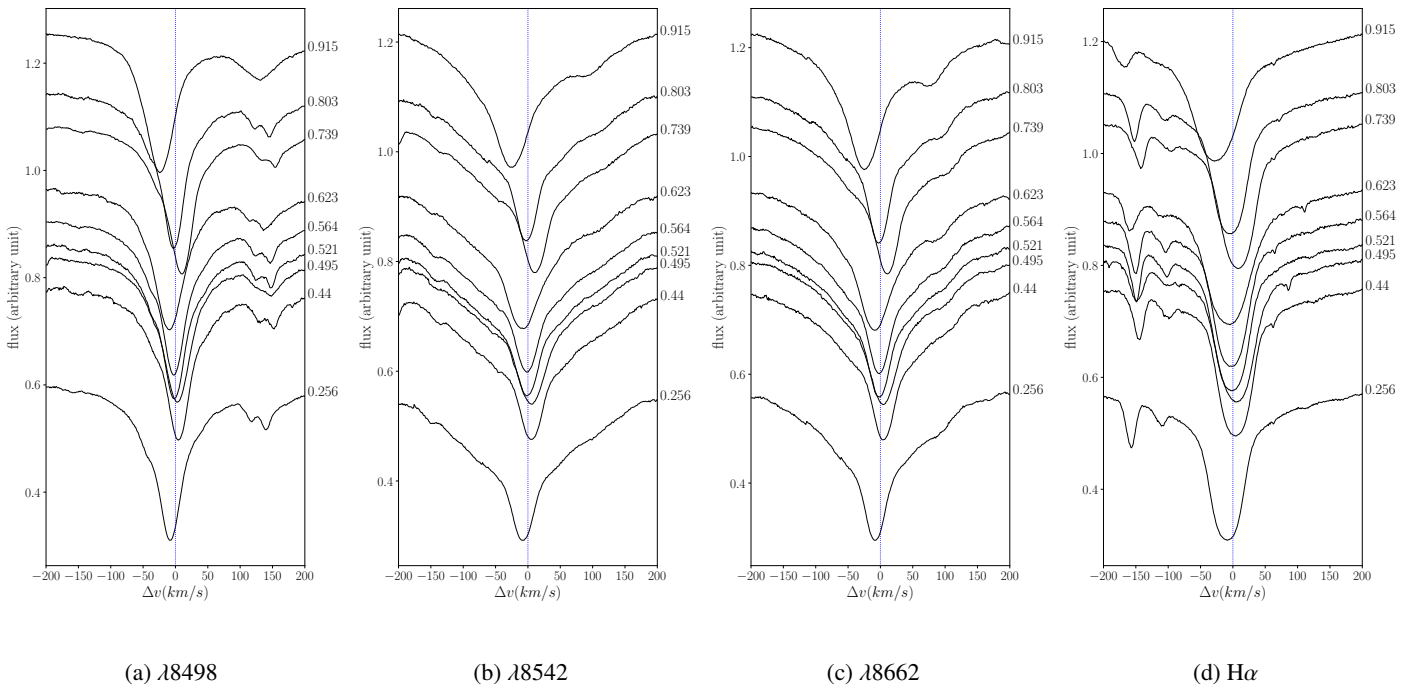


Fig. B.6: EW Sct, 5.82d

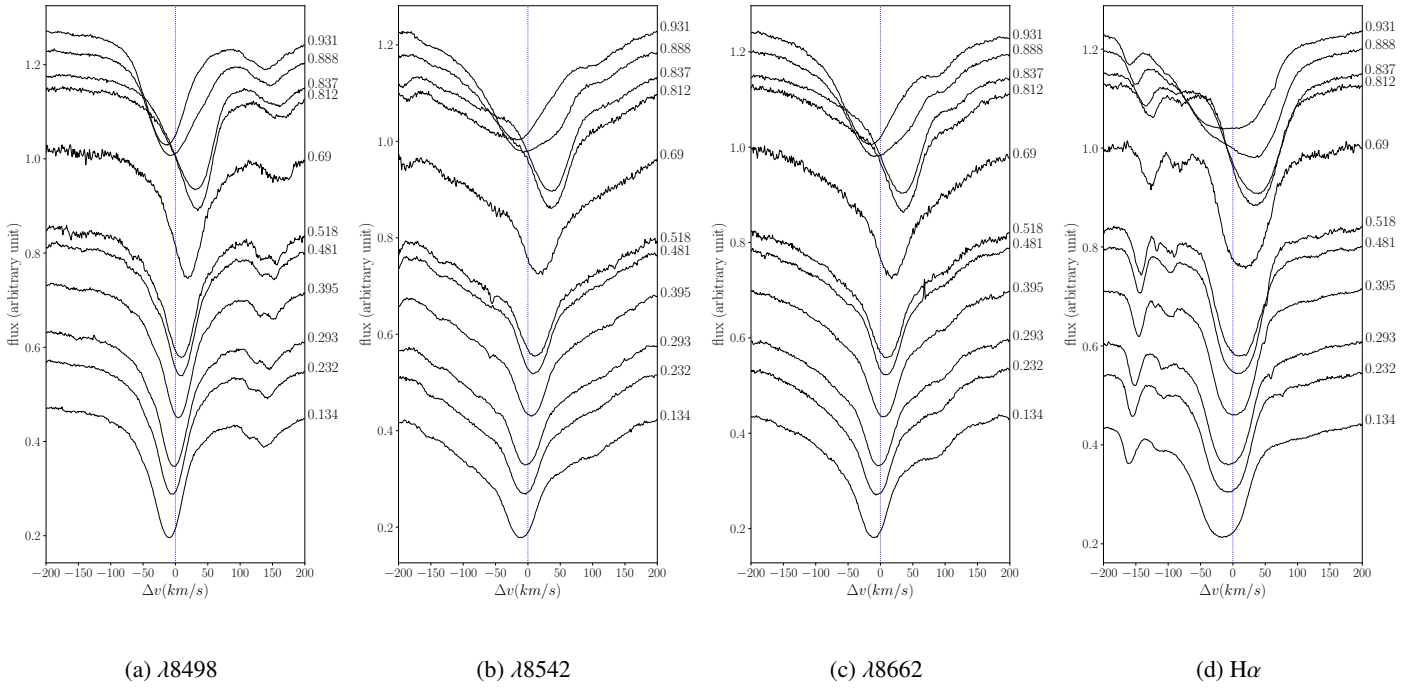


Fig. B.7: U Sgr, 6.75d

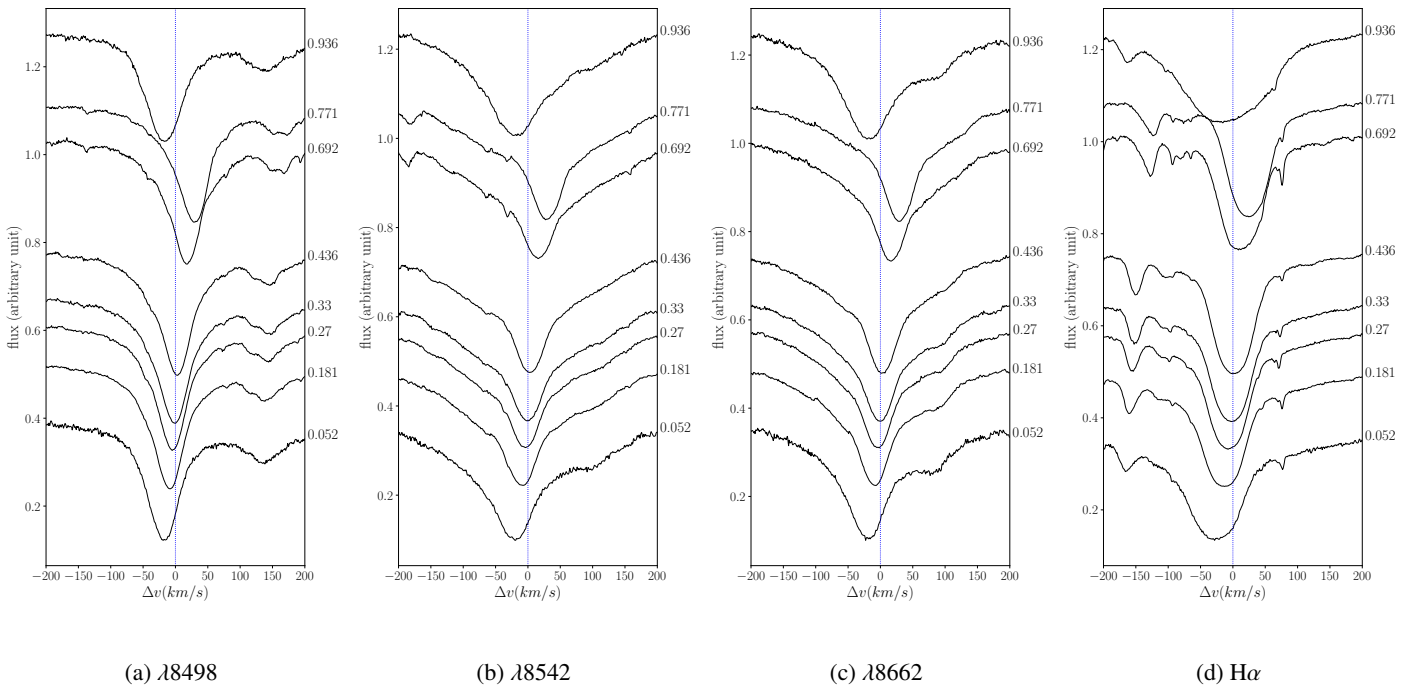


Fig. B.8: R Mus, 7.51d

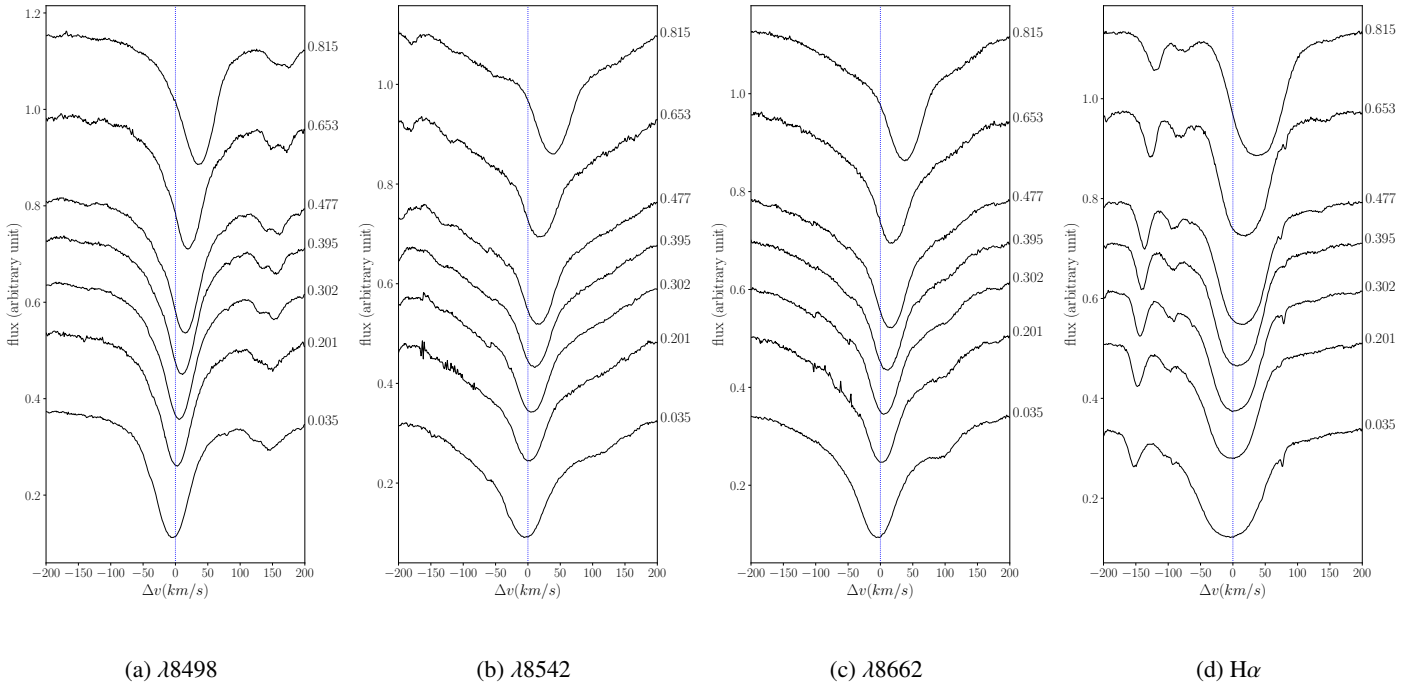


Fig. B.9: V636 Sco, 7.8d

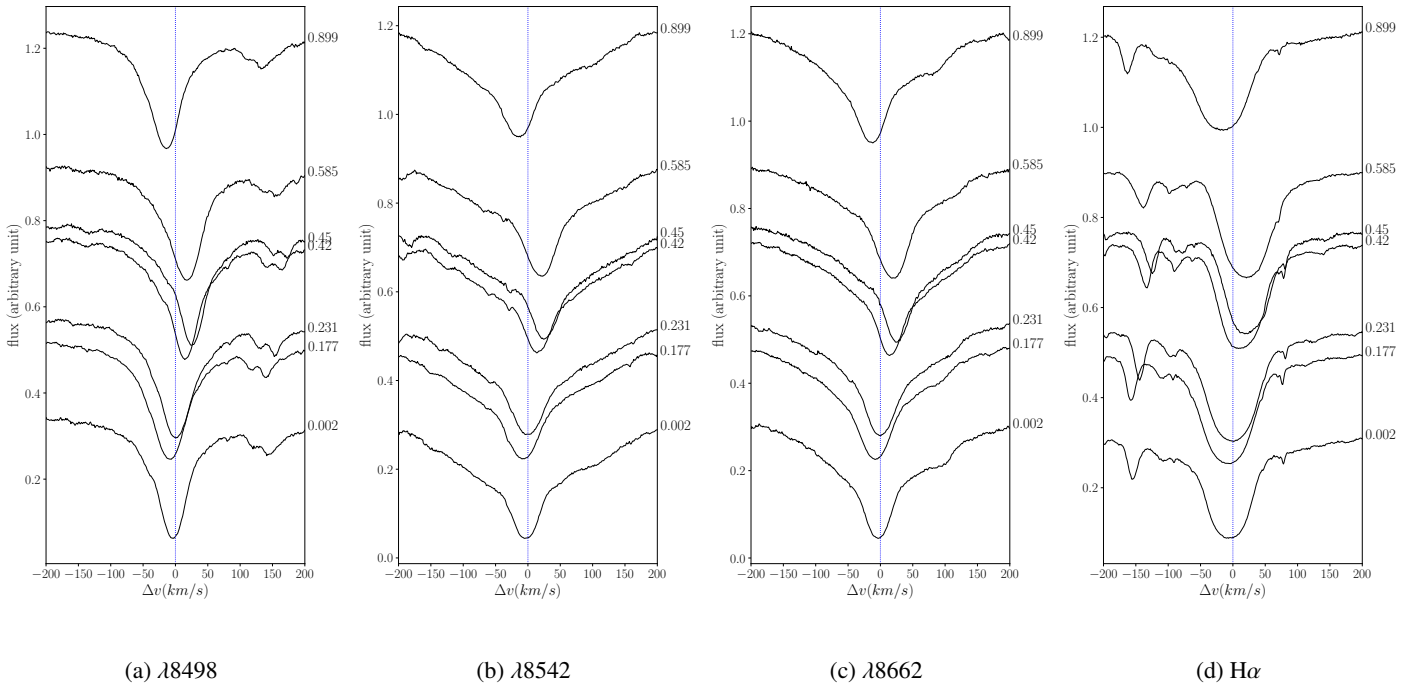


Fig. B.10: S Mus, 9.66d

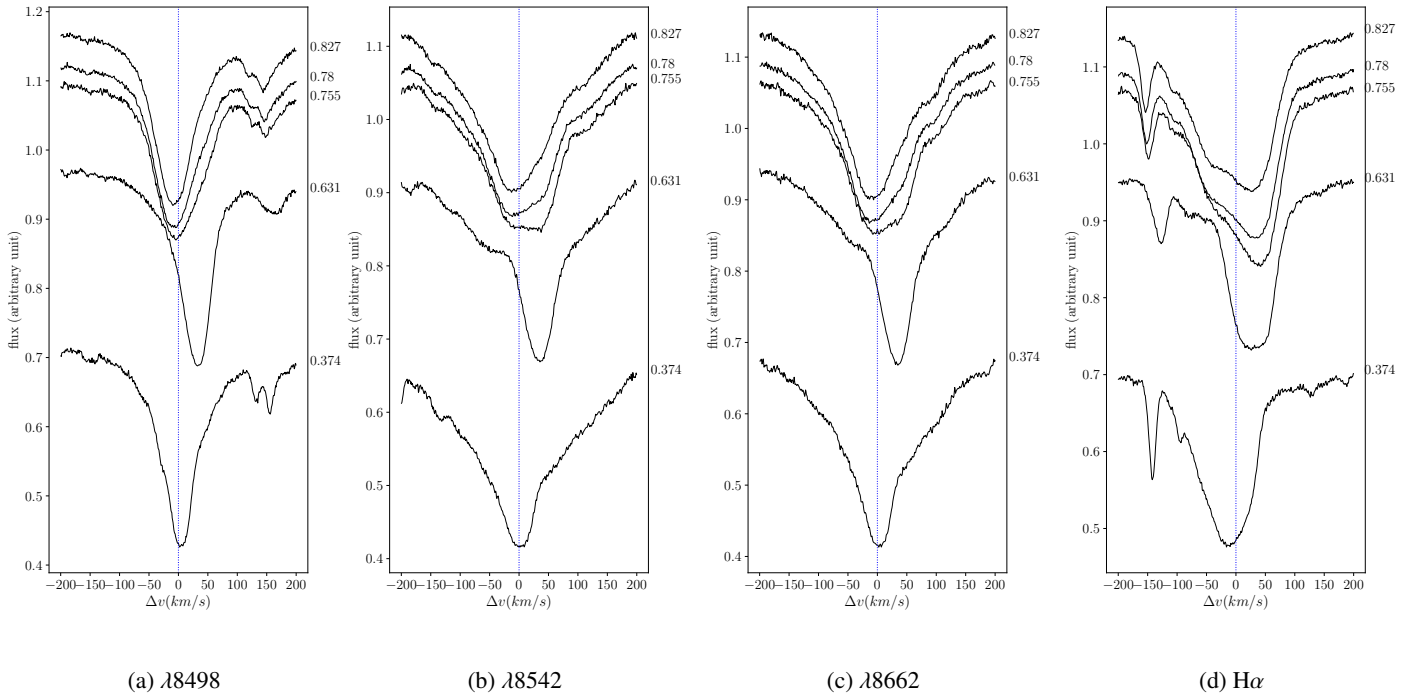


Fig. B.11: β Dor, 9.84d

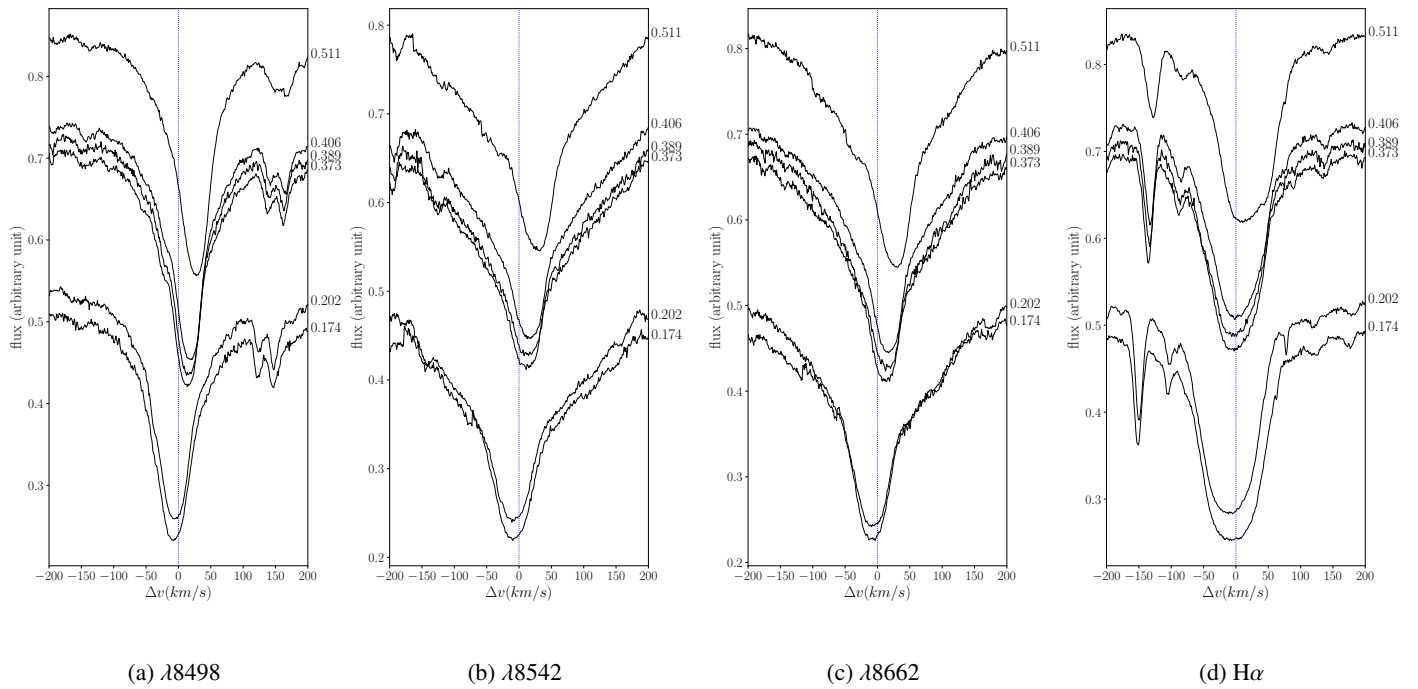


Fig. B.12: ζ Gem, 10.15d

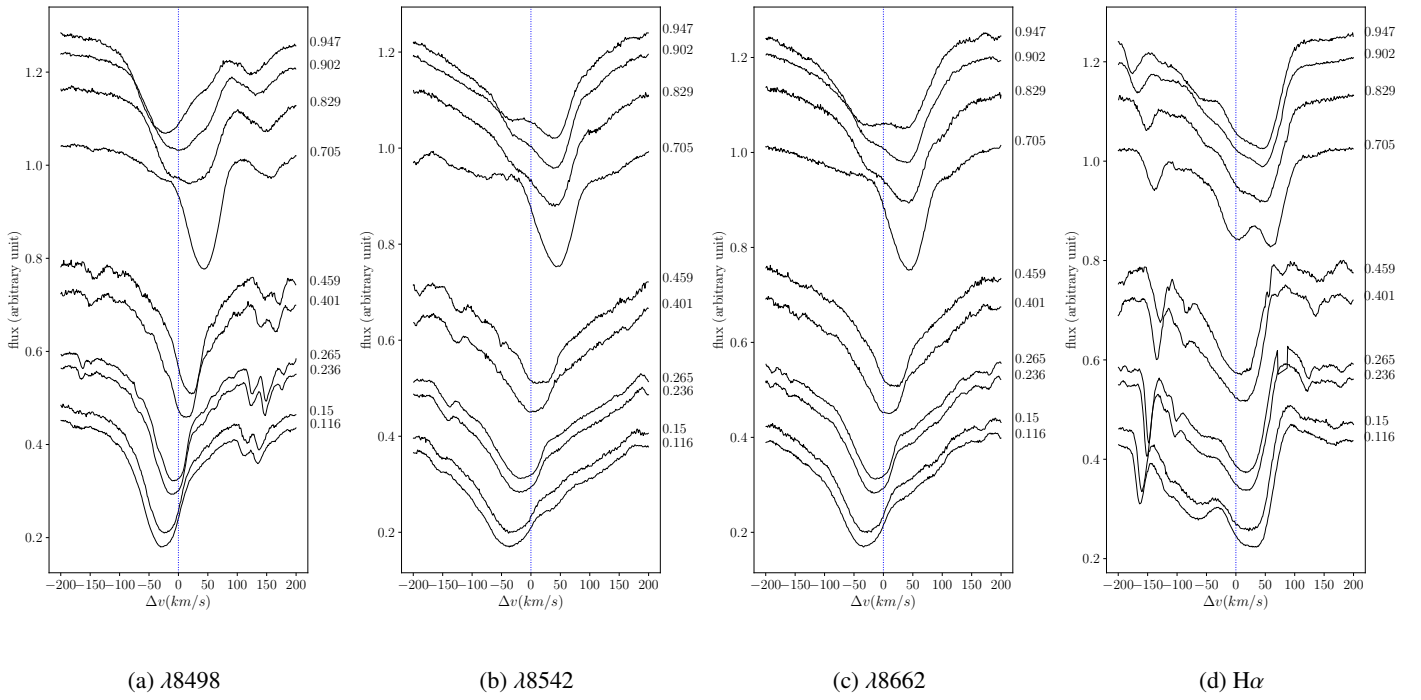


Fig. B.13: TT Aql, 13.75d

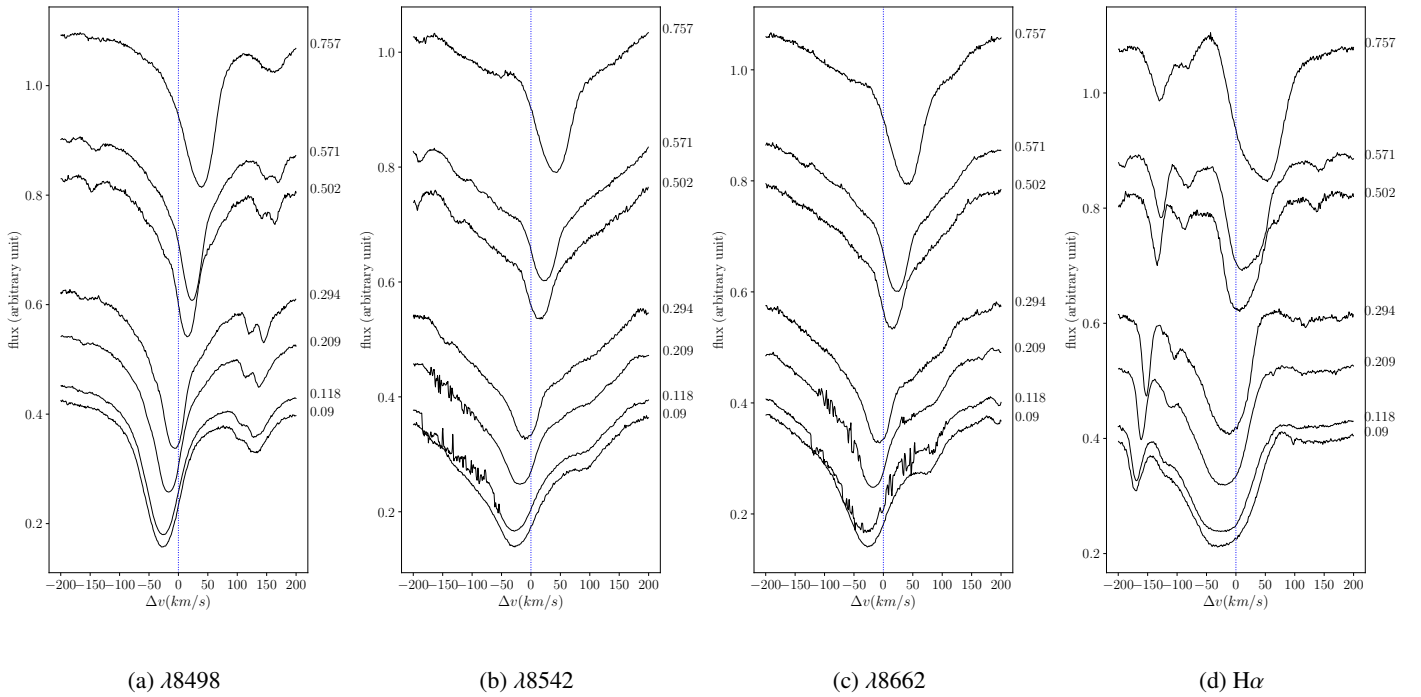


Fig. B.14: RU Sct, 19.70d

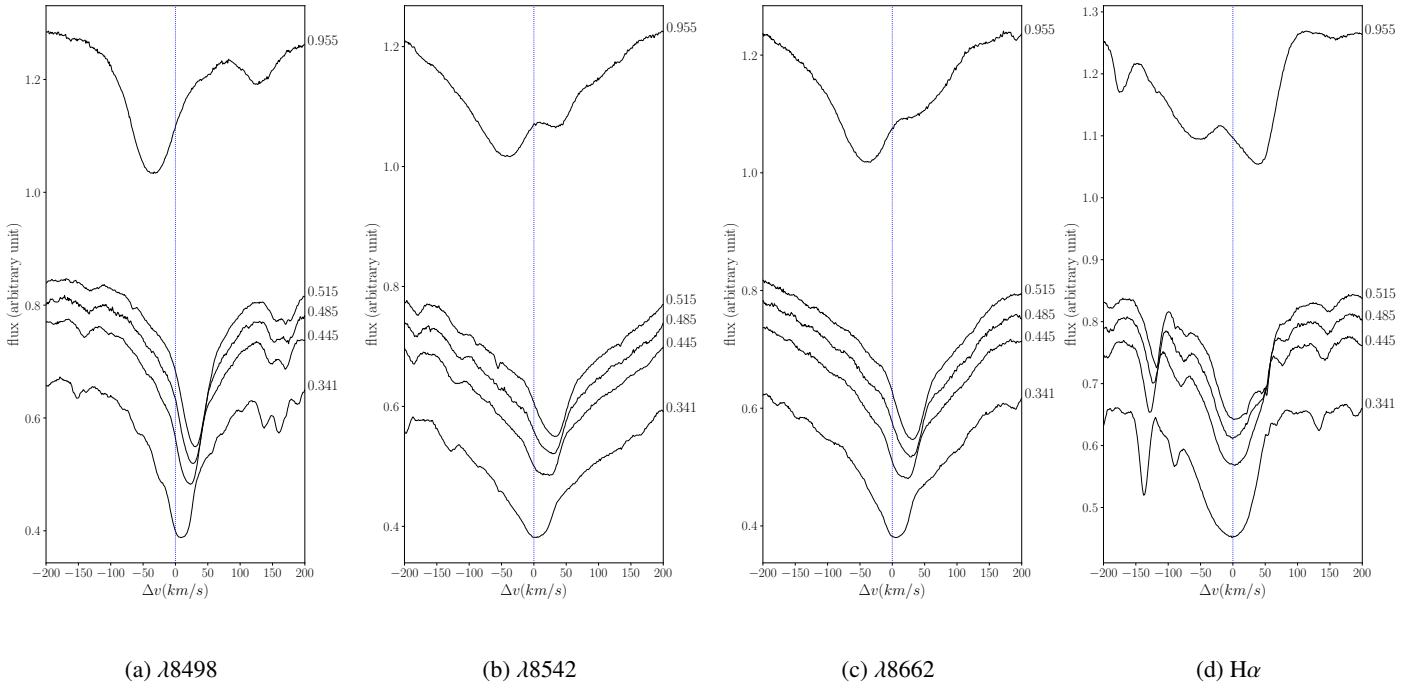


Fig. B.15: RZ Vel, 20.39d

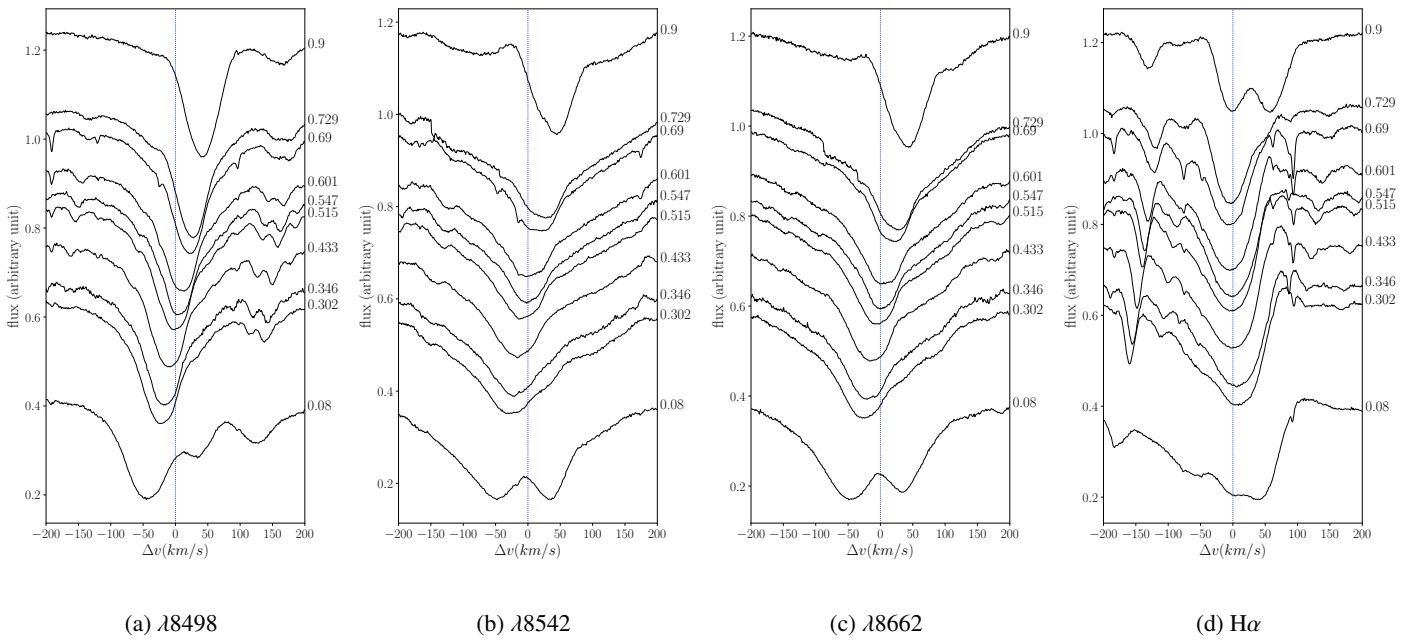


Fig. B.16: WZ Car, 23.01d

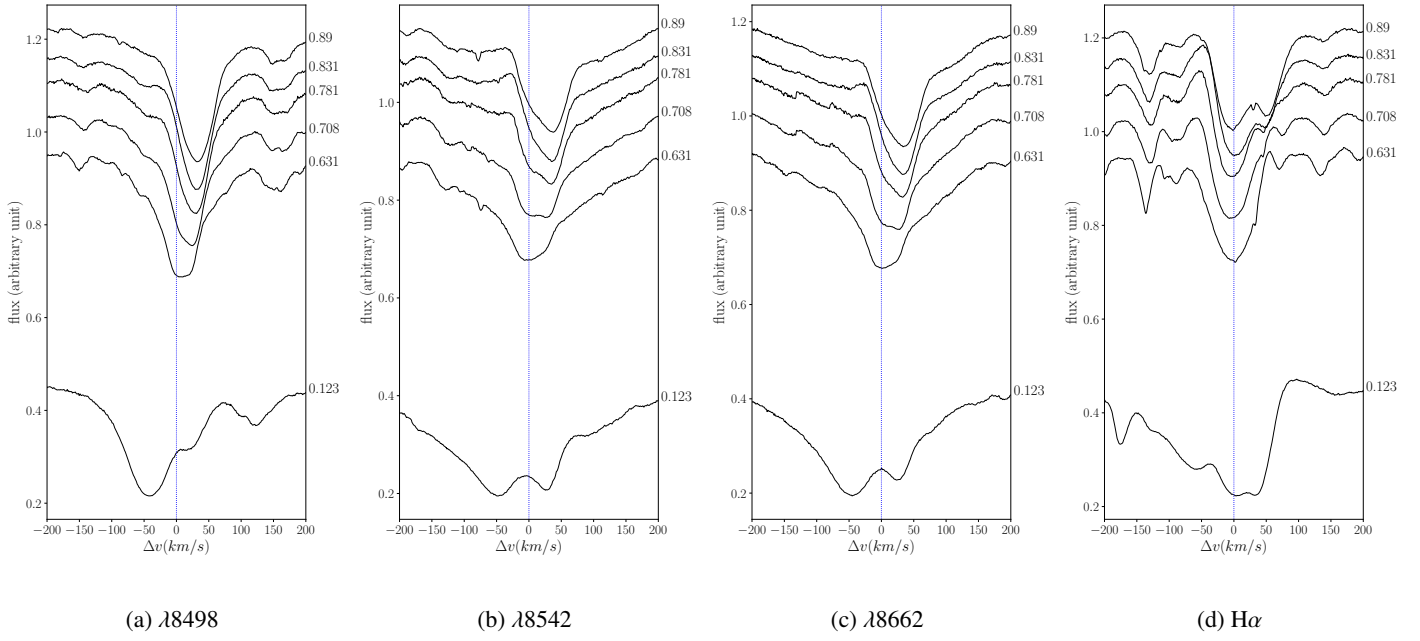


Fig. B.17: T Mon, 27.02d

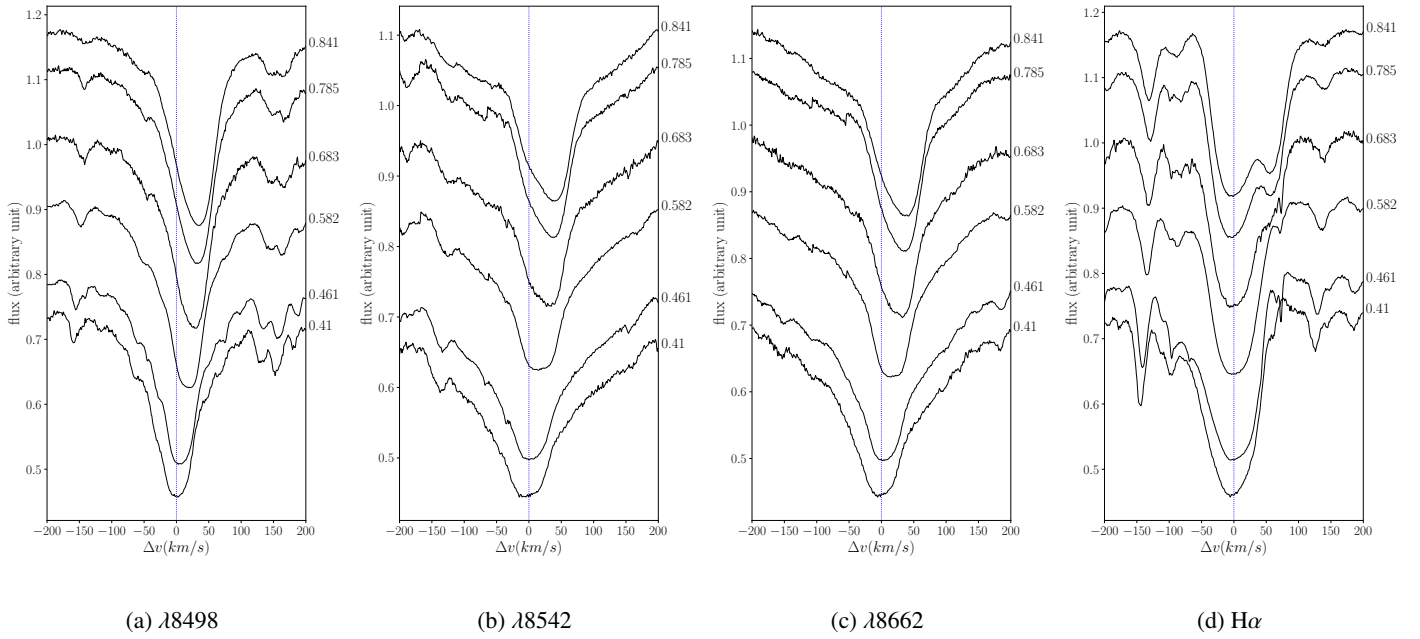


Fig. B.18: l Car, 35.55d

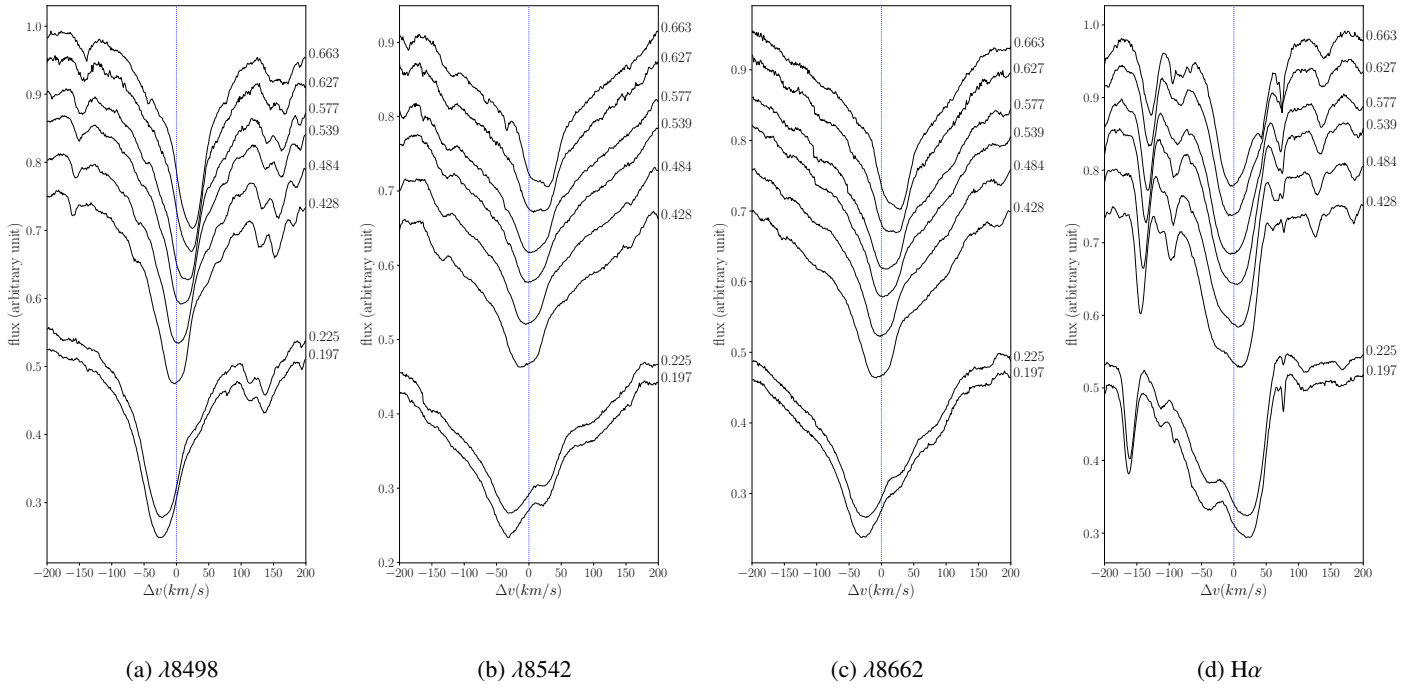


Fig. B.19: U Car, 38.80d

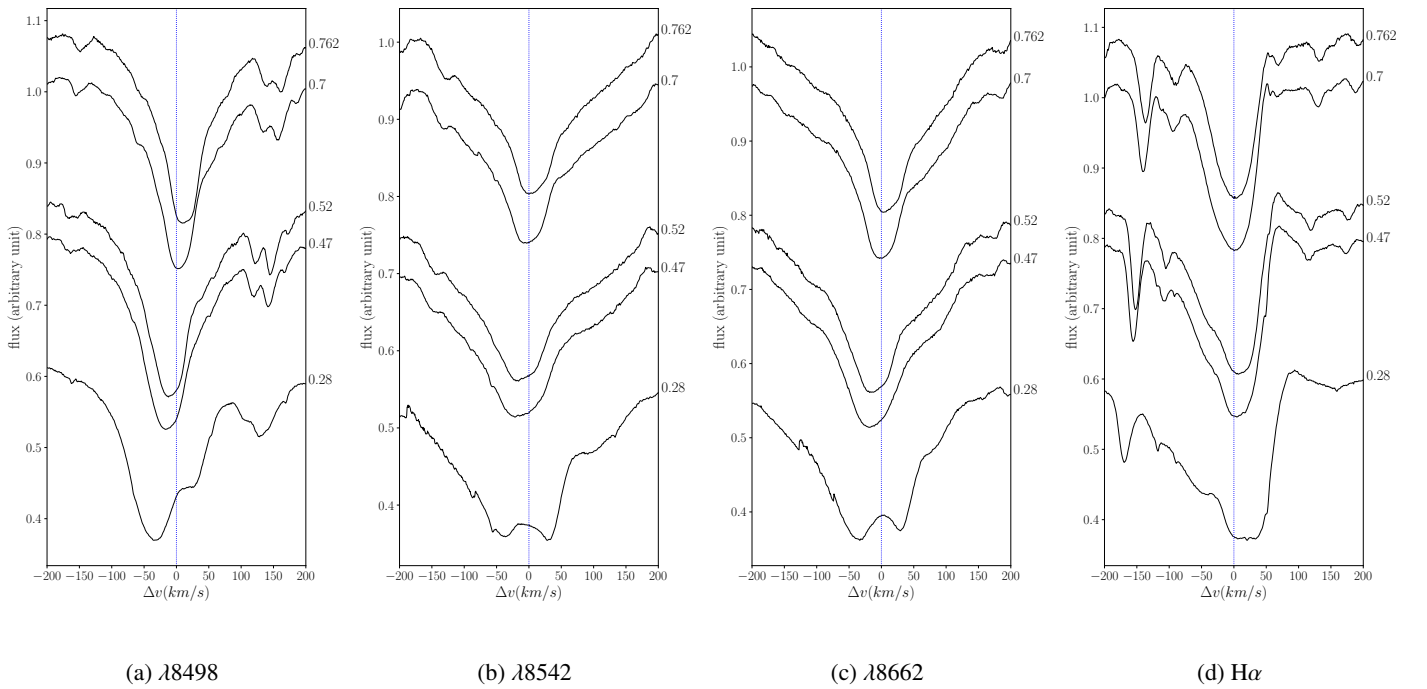


Fig. B.20: RS Pup, 41.46d

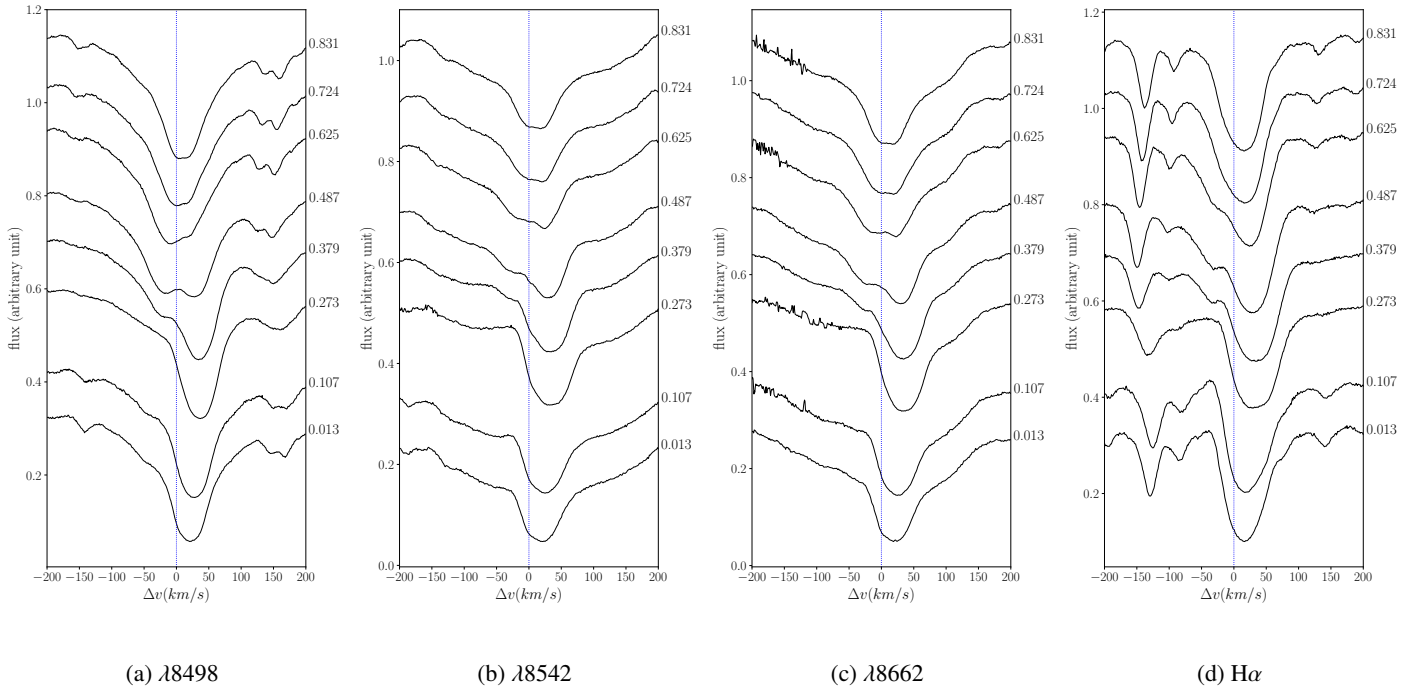


Fig. B.21: V1496 Aql, 65.37d